PROCEEDINGS OF THE ROYAL SOCIETY A MATHEMATICAL, PHYSICAL & ENGINEERING SCIENCES

A depth-averaged debris-flow model that includes the effects of evolving dilatancy. I. Physical basis

Richard M. Iverson and David L. George

Proc. R. Soc. A 2014 **470**, 20130819, published 30 July 2014

PROCEEDINGS OF THE ROYAL SOCIETY A

rspa.royalsocietypublishing.org

A depth-averaged debris-flow model that includes the effects of evolving dilatancy. I. Physical basis

Richard M. Iverson and David L. George

US Geological Survey, 1300 SE Cardinal Ct. Vancouver, WA 98683, USA

Research

Cite this article: Iverson RM, George DL. 2014 A depth-averaged debris-flow model that includes the effects of evolving dilatancy. I. Physical basis. *Proc. R. Soc. A* **470**: 20130819. http://dx.doi.org/10.1098/rspa.2013.0819

Received: 10 December 2013
Accepted: 30 June 2014

Subject Areas:
geophysics, fluid mechanics, volcanology

Keywords:
debris flow, dilatancy, modelling

Author for correspondence:
Richard M. Iverson
e-mail: riverson@usgs.gov

To simulate debris-flow behaviour from initiation to deposition, we derive a depth-averaged, two-phase model that combines concepts of critical-state soil mechanics, grain-flow mechanics and fluid mechanics. The model's balance equations describe coupled evolution of the solid volume fraction, m, basal pore-fluid pressure, flow thickness and two components of flow velocity. Basal friction is evaluated using a generalized Coulomb rule, and fluid motion is evaluated in a frame of reference that translates with the velocity of the granular phase, $\boldsymbol{v}_s$. Source terms in each of the depth-averaged balance equations account for the influence of the granular dilation rate, defined as the depth integral of $\nabla \cdot \boldsymbol{v}_s$. Calculation of the dilation rate involves the effects of an elastic compressibility and an inelastic dilatancy angle proportional to $m - m_{eq}$, where m_{eq} is the value of m in equilibrium with the ambient stress state and flow rate. Normalization of the model equations shows that predicted debris-flow behaviour depends principally on the initial value of $m - m_{eq}$ and on the ratio of two fundamental timescales. One of these timescales governs downslope debris-flow motion, and the other governs pore-pressure relaxation that modifies Coulomb friction and regulates evolution of m. A companion paper presents a suite of model predictions and tests.

1. Introduction

Debris flows are water-saturated masses of soil and fragmented rock that rush down mountainsides, funnel into stream channels and form lobate deposits when they spill onto valley floors. Their geological nature and mechanical behaviour make them intermediate in character between rock avalanches and flash floods.

Royal Society Publishing

Figure 1. Oblique aerial photograph of source areas and runout paths of devastating debris flows that occurred in a densely populated region of Vargas state east of Macuto, Venezuela, December, 1999. Photograph by Matthew Larsen, US Geological Survey.

Because debris flows have solid grain concentrations that exceed 0.4, peak speeds that commonly surpass 10 m s^{-1}, and volumes that range up to approximately 10^9 m^3, they can denude slopes, bury floodplains and devastate people and property [1,2]. Notable recent debris-flow disasters involved more than 20 000 fatalities in Armero, Columbia, in 1985 and in Vargas state, Venezuela, in 1999 (figure 1).

Alternative terms such as mudflow, mudslide, debris torrent and lahar are sometimes used to describe debris flows, but the terms 'debris' and 'flow' have precise geological meanings. 'Debris' implies that grains with greatly differing sizes and irregular shapes are present. This trait—and the consequent lack of a characteristic grain size—distinguishes debris-flow mixtures from most man-made granular mixtures. In debris flows, the largest grains can have linear dimensions exceeding 10 m, but the presence of at least several weight per cent mud-sized particles smaller than about 62 μm is generally more critical [3]. Hydrodynamic suspension of these small particles increases the effective viscosity of the muddy water that fills pore spaces between larger grains [4], and this enhanced viscosity can promote development and persistence of high pore-fluid pressure that facilitates debris-flow motion by reducing grain contact forces [5–7]. The term 'flow' implies that rearrangement of grain contacts is pervasive during debris-flow motion. Indeed, granular debris that is liquefied by high pore-fluid pressure can appear to flow almost as fluidly as water [8].

Spatial and temporal changes in macroscopic material behaviour that result from local rearrangements of grains and attendant evolution of pore-fluid pressure pose fundamental challenges for continuum mechanical modelling of debris flows. The most conspicuous transitions occur as debris mobilizes from static material on slopes, liquefies and flows rapidly, and later regains rigidity during consolidation of deposits [9,10]. Most debris-flow models neglect these transitions, and instead treat rheology or depth-averaged flow resistance as inherent properties of debris [11]. With this approach, flow dynamics simulations typically employ basal flow resistance coefficients less than half as large as those necessary to statically balance forces at flow initiation sites [12–14]. Unbalanced initial states are held in check by assuming that an imaginary dam restrains the debris until the modeller issues a command, but use of this type of initial condition compromises physical relevance.

By contrast, most natural debris flows commence when balanced forces are infinitesimally perturbed. Flow onset commonly results from rainfall or snowmelt that triggers failure of debris-mantled slopes or mobilization of scree in steep rills and gullies. As masses of water-saturated grains begin to move, however, the governing force imbalance can evolve dramatically owing to pore-pressure feedbacks that modify the apparent rheology of the debris [15–17]. Differences between this type of behaviour and behaviour that arises from a stipulated rheology and force imbalance have great practical as well as theoretical significance, because pore-pressure feedbacks can determine whether a rapid debris flow develops at all—as opposed to a creeping landslide that moves imperceptibly or intermittently downslope [18,19].

2. Objectives

Our chief goal is seamless simulation of debris-flow motion from initiation to deposition without any redefinition of governing equations, re-evaluation of parameters or restructuring of numerical methods. An ancillary goal is efficient machine computation of solutions for use in practical applications. We pursue these goals by formulating a depth-averaged model that allows feedbacks to develop during coupled evolution of solid and fluid volume fractions, pore-fluid pressure and debris-flow velocity and thickness. The feedbacks involve dilatancy – the state-dependent propensity of granular materials to undergo changes in solid volume fraction as they shear. Well-known since the time of Reynolds [20,21], variable dilatancy underpins the critical-state theory of soil mechanics [22–24], and it plays a key role in determining of the continuum-scale rheology of dense granular flows [25].

Previous depth-averaged debris-flow models have included effects of solid–fluid interactions, and a few have accounted for evolution of solid and fluid volume fractions [5,26–35]. However, no previous model has explicitly considered dilatancy coupled to pore-pressure feedbacks that mediate transitions between static and dynamic states. Dry granular materials can undergo analogous state transitions [36], which can be characterized by using a continuum mechanical model that employs an evolving order parameter to account for changes in mobility due to changes in solid volume fraction [37]. The order parameter is not physically measurable, however. By contrast, direct measurements of pore-pressure evolution due to variable dilatancy have led to development of a model that successfully simulates a transition from failure to flow that occurs when water-saturated granular avalanches are manually triggered by increasing the steepness of submerged slopes [38]. Additional experiments with concentrated grain–fluid mixtures have shown that a state-dependent Coulomb friction rule that embeds the effects of variable dilatancy can successfully describe bulk flow resistance over a broad range of normalized shear rates, including quasi-static rates [39]. Our model is founded partly on these findings.

All physical principles and empiricisms used in our model are implemented within a depth-averaged framework. Use of depth-averaged equations in conjunction with shock-capturing numerical methods and adaptive mesh refinement yields a combination of computational speed and accuracy well suited for assessment of diverse flow hazards [40,41]. Like all depth-averaged models, however, our model neglects some details of three-dimensional behaviour. It nevertheless provides predictions that can be rigorously tested because it computes flow depths, velocities and basal pore pressures with a resolution similar to that of the most-detailed debris-flow data collected to date [10,16,42–45]. Use of the solid volume fraction as an additional prognostic variable expands the possibilities for future model tests.

Section 3 describes physical principles and observations that guide formulation of our model. Subsequent sections describe derivation of the depth-averaged model equations and analytical results that help clarify their physical implications. A companion paper [46] examines mathematical properties of the model, describes our numerical method for solving the model equations, and tests computational predictions of initiation of debris-flow motion as well as subsequent flow and deposition.

3. Physical principles and definitions

To represent debris-flow behaviour, our model combines principles from soil mechanics, grain-flow mechanics and fluid mechanics, which we quantify below. We also quantify our rationale for treating two-phase debris flows as granular flows with evolving solid volume fractions and pore-fluid pressures. In this approach the fluid-phase velocity is evaluated in a frame of reference that translates with the granular phase, and variations of fluid velocity result in variations of fluid pressure. Our model excludes the effects of grain-size segregation and bed-sediment entrainment, which are important in many debris flows [44,47]. It is designed to incorporate the effects of segregation and entrainment in a manner consistent with the depth-integrated analyses of Gray & Kokelaar [48] and Iverson [49], however.

(a) Continuum conservation laws

Within each phase of a debris-flow mixture, and also within the mixture as a whole, conservation of mass is expressed by

$$\frac{\partial \rho}{\partial t} + \nabla \cdot \rho \boldsymbol{v} = 0, \tag{3.1}$$

where ρ is the mass density and $\boldsymbol{v}$ is the velocity vector. Similarly, conservation of linear momentum is expressed by

$$\frac{\partial \rho \boldsymbol{v}}{\partial t} + \nabla \cdot \rho \boldsymbol{v}\boldsymbol{v} = \rho \boldsymbol{g} + \nabla \cdot T, \tag{3.2}$$

where $\boldsymbol{g}$ is the acceleration due to gravity and T is the stress tensor, which is assumed to be symmetric [50]. We use the standard sign convention of continuum mechanics to define shear components of T [51,52]. However, because granular debris can sustain negligible tension, we define normal components of T using a soil mechanics sign convention in which compressive stresses are positive. Thus, in rectangular Cartesian coordinates we express the x component of $\nabla \cdot T$ as $-\partial \tau_{xx}/\partial x + \partial \tau_{yx}/\partial y + \partial \tau_{zx}/\partial z$. Use of this convention simplifies our definition of constitutive equations and evaluation of boundary tractions.

Our model includes no energy-conservation equation because we treat debris flows as isothermal systems. By contrast, Bartelt *et al.* [53] have developed a depth-averaged model of granular snow avalanches that includes an energy equation roughly analogous to those used in kinetic grain-flow theories. In the model of Bartelt *et al.* [53], the effective frictional resistance of an avalanche evolves because it is mediated by evolution of kinetic energy associated with grain velocity fluctuations. The effective frictional resistance evolves in our model as well, but it does so as a result of evolution of dilatancy and pore-fluid pressure. The difference between our formulation and that of Bartelt *et al.* [53] is logical, because debris flows contain muddy pore water that is roughly 10^3 times more dense and viscous, as well as 10^4 times less compressible, than pore air at Earth's surface. Therefore, as demonstrated by dimensional analysis, pore fluid is likely to play a pivotal role in debris flows but not in most dry avalanches [54].

(b) Definitions of volume fractions, densities and velocities

Our model assumes that the solid and fluid constituents of debris are incompressible, with mass densities ρ_s and ρ_f, respectively. Therefore, the mixture bulk density ρ varies exclusively as a result of grain rearrangements and elastic shear distortion localized at grain contacts (cf. [55]). Our definition of the mixture bulk density,

$$\rho = \rho_s m + \rho_f (1 - m), \tag{3.3}$$

additionally assumes that each representative elementary volume of debris contains sufficient solid and fluid material that the solid volume fraction m and fluid volume fraction $1 - m$ can be regarded as continuous variables. Commonly m varies from about 0.4 in the most dilute debris flows (or parts of debris flows) to 0.8 in the densest (cf. [56]). This variation implies that ρ ranges

from about 1700 to 2400 kg m^{-3}, because the solid constituents of debris are largely rock fragments with $\rho_s \approx 2700\,\mathrm{kg\,m^{-3}}$, and the fluid constituents are mostly muddy water with ρ_f ranging from about 1000 to 1200 kg m^{-3} [5,57].

Like the mixture density, the mixture momentum is weighted by the mass of solid grains $\rho_s m$ and mass of pore fluid $\rho_f(1-m)$ per unit volume, but it also depends on the velocities of each phase. Thus, the linear momentum of the mixture is defined as $\rho \boldsymbol{v} = \boldsymbol{v}_s \rho_s m + \boldsymbol{v}_f \rho_f (1-m)$, where $\boldsymbol{v}_s$ is the velocity of the solid grains, and $\boldsymbol{v}_f$ is the velocity of the pore fluid. This definition of mixture momentum implies that the mixture velocity is defined as

$$\boldsymbol{v} = \frac{\boldsymbol{v}_s \rho_s m + \boldsymbol{v}_f \rho_f (1-m)}{\rho}. \tag{3.4}$$

Another velocity that plays a key role in our model is the pore-fluid velocity relative to the solid grain velocity, $\boldsymbol{v}_f - \boldsymbol{v}_s$. To an observer moving with the local solid velocity $\boldsymbol{v}_s$, the apparent fluid velocity is the volumetric flux of pore fluid per unit area of mixture, $\boldsymbol{q}$:

$$\boldsymbol{q} = (1-m)(\boldsymbol{v}_f - \boldsymbol{v}_s). \tag{3.5}$$

In porous media theory, $\boldsymbol{q}$ is termed the specific discharge [58].

To simplify our model, we approximate the mixture velocity as $\boldsymbol{v} \approx \boldsymbol{v}_s$. The basis for this approximation can be established by using (3.3)–(3.5) to find that

$$\frac{\boldsymbol{v}}{\|\boldsymbol{v}_s\|} = \frac{\rho_f}{\rho}\frac{\boldsymbol{q}}{\|\boldsymbol{v}_s\|} + \frac{\boldsymbol{v}_s}{\|\boldsymbol{v}_s\|}, \tag{3.6}$$

where $\|\ \|$ denotes the Euclidean norm of a vector. For rapid debris-flow motion, (3.6) reduces to $\boldsymbol{v} \approx \boldsymbol{v}_s$, because values $\rho_f/\rho \approx 1/2$ and $\|\boldsymbol{q}\|/\|\boldsymbol{v}_s\| \ll 1$ are typical [5]. For the initial and final stages of debris-flow motion, with $\|\boldsymbol{v}_s\| \approx 0$, (3.6) instead reduces to $\boldsymbol{v} \approx (\rho_f/\rho)\boldsymbol{q}$. Nevertheless, $\boldsymbol{v} \approx \boldsymbol{v}_s$ remains a good approximation because $\|\boldsymbol{q}\| \ll 0.1\,\mathrm{m\,s^{-1}}$ is typical, implying that the mixture momentum balance (3.2) reduces to the quasi-static form $\rho \boldsymbol{g} + \nabla \cdot T \approx 0$ [59].

(c) Definitions of total stress, effective stress and pore-fluid pressure

A formulation that approximates the mixture momentum as $\rho \boldsymbol{v}_s$ requires that the total mixture stress T must account not only for solid- and fluid-phase stresses but also for all effects of solid–fluid interactions. These effects can be diverse, but in mixtures of fluid and macroscopic grains (subject to negligible Brownian forces), the effects are commonly dominated by buoyancy and viscous drag [33,60]. Other interaction forces include hydrodynamic-lift, added-mass and Basset forces, but these forces are probably muted in debris flows owing to restriction of fluid flow caused by high concentrations of grains with differing shapes and sizes [5,6]. Indeed, a linear Darcian drag law can explain relaxation of non-hydrostatic pore-pressure gradients measured in freshly agitated, liquefied debris-flow slurries [61]. On this basis, our model assumes that buoyancy and viscous drag wholly account for the effects of solid–fluid interactions on the mixture stress, T. As shown below, the net effect of these interactions is manifested on a bulk continuum scale by gradients of pore-fluid pressure, p.

Our model isolates the effects of p by using a principle of soil mechanics, which states that T can be expressed as the sum of p and an effective stress T_e [55,62]. By convention T_e and p are treated mathematically as if they act throughout the entire solid–fluid mixture, although this practice is largely a matter of convenience and is not mandated by mechanics [63,64]. By combining T_e and p with a viscous deviatoric stress component T_{vis} (which acts only in the fluid volume fraction $1-m$ as a result of shearing of the fluid phase), we define the total mixture stress as

$$T = T_e + Ip + (1-m)T_{vis}, \tag{3.7}$$

where I is the identity tensor. Equation (3.7) indicates that, in the presence of constant T, increases in p cause commensurate reductions in the mean effective normal stress σ_e, defined as

$$\sigma_e = \tfrac{1}{3}\mathrm{tr}(T_e) = \tfrac{1}{3}\mathrm{tr}(T) - p = \sigma - p, \tag{3.8}$$

where $\sigma = (1/3)\mathrm{tr}(T)$ is the mean total normal stress.

To distinguish the effects of buoyancy from those of solid–fluid drag, we subdivide p into a hydrostatic component p_h and a non-hydrostatic 'excess' component p_e

$$p = p_h + p_\mathrm{e}. \tag{3.9}$$

In our model, values of p_h depend only on the evolving geometry of a mass of fluid-saturated debris, whereas values of p_e are affected by $\boldsymbol{q}$. In turn, $\boldsymbol{q}$ is a consequence of debris dilation or contraction.

(d) Definition of dilation rate

We define the local debris dilation rate as the divergence of $\boldsymbol{v}_\mathrm{s}$, which is related to evolution of the solid volume fraction m by

$$\nabla \cdot \boldsymbol{v}_\mathrm{s} = -\frac{1}{m}\frac{\mathrm{d}m}{\mathrm{d}t}, \tag{3.10}$$

where $\mathrm{d}/\mathrm{d}t = \partial/\partial t + \boldsymbol{v}_\mathrm{s} \cdot \nabla$ is a material time derivative in a frame of reference that moves with the granular velocity $\boldsymbol{v}_\mathrm{s}$ [58]. Thus, $\mathrm{d}m/\mathrm{d}t < 0$ indicates a positive dilation rate, whereas $\mathrm{d}m/\mathrm{d}t > 0$ indicates a negative dilation rate (i.e. a rate of contraction). Although $\nabla \cdot \mathrm{v}_\mathrm{s}$ does not appear explicitly in our final model equations, $\mathrm{d}m/\mathrm{d}t$ plays a prominent role.

Because we assume that incompressible fluid fills all pore spaces in the debris (except where grains may protrude from the free upper surface of a flow, as detailed in §4), the debris dilation rate is locally balanced by the divergence of $\boldsymbol{q}$. This fact can be demonstrated formally by manipulating the mixture mass-conservation equation (3.1) while embedding the definitions (3.3)–(3.5) to obtain

$$\nabla \cdot \boldsymbol{v}_\mathrm{s} = -\nabla \cdot \boldsymbol{q}. \tag{3.11}$$

Thus, a positive dilation rate is accompanied by a local influx of fluid, and a negative dilation is accompanied by a local fluid efflux.

A central postulate of our model is that the dilation rate depends on two mechanical phenomena that modify m: changes in σ_e that cause reduction or enlargement of the debris pore space due to bulk compressibility of the mixture, and changes in mixture shear strain that cause pore space contraction or expansion due to dilatancy. We assume that these two phenomena are independent of one another, except insofar as they each involve interactions with other variables such as pore-fluid pressure. We therefore define the total rate of change of m as

$$\frac{\mathrm{d}m}{\mathrm{d}t} = \frac{\partial m}{\partial \sigma_\mathrm{e}}\frac{\mathrm{d}\sigma_\mathrm{e}}{\mathrm{d}t} + \frac{\partial m}{\partial \dot{\gamma}}\dot{\gamma}, \tag{3.12}$$

where γ is a scalar measure of natural shear strain, which is referenced to evolving granular-phase material coordinates that move with velocity $\boldsymbol{v}_\mathrm{s}$ (cf. [52, p. 151]), and $\dot{\gamma} = \mathrm{d}\gamma/\mathrm{d}t$ is a scalar measure of the associated shear rate (i.e. $\dot{\gamma}/2$ is the square root of the second principal invariant of the deviatoric deformation-rate tensor). A detailed description of three-dimensional strains and deformation rates is beyond the scope of our depth-averaged model, however, and is also beyond the resolution limits of the most-detailed full-scale debris-flow experiments conducted to date [9,16,44,65,66]. Therefore, we estimate the effects of $\dot{\gamma}$ on $\mathrm{d}m/\mathrm{d}t$ by considering idealized deformations consisting of isotropic volume strain and homogeneous simple shearing in $x - z$ and/or $y - z$ planes (figure 2). This idealization yields a parsimonious model that can be tested using existing datasets [46].

(e) Definition of compressibility

Application of (3.12) requires a constitutive relationship to determine $\partial m/\partial \sigma_\mathrm{e}$. At effective confining stresses typical of debris flows less than 50 m thick ($\sigma_\mathrm{e} \leq 10^6$ Pa), bulk compression or expansion of granular debris caused by changes in σ_e results almost entirely from changes in pore volume rather than from changes in the densities of the debris' solid and fluid constituents

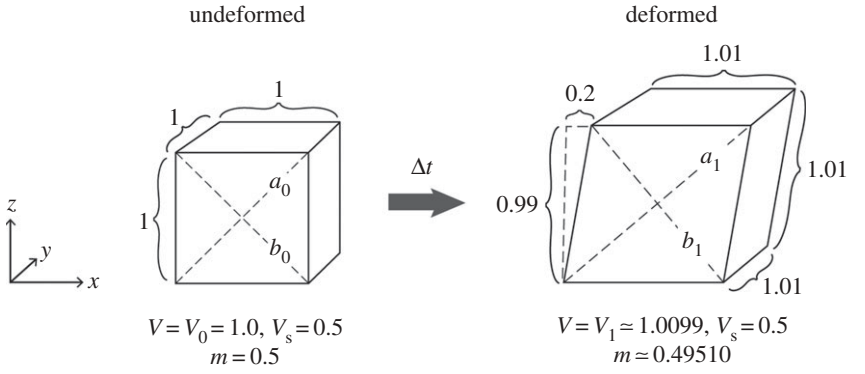

Figure 2. Idealized deformation of a cubical unit cell subject to isotropic dilation (exaggerated for illustrative purposes) and homogeneous simple shearing in the x–z plane during the time increment Δt. Volume of solid grains in unit cell, V_s, is the same in undeformed and deformed states, but changes occur in total cell volume, V, and solid volume fraction, $m = V_s/V$. Major and minor principal components of cumulative natural strain depicted in this example are $\varepsilon_1 = \ln(a_1/a_0) \approx 0.10028$ and $\varepsilon_3 = \ln(b_1/b_0) \approx -0.10038$. Cumulative intermediate principal strain (normal to page) is $\varepsilon_2 = \ln(1.01/1) \approx 0.009950$, cumulative shear strain is $\varepsilon_1 - \varepsilon_3 \approx 0.20066$ and cumulative volume strain is $\varepsilon_V = \ln(V_1/V_0) = \varepsilon_1 + \varepsilon_2 + \varepsilon_3 \approx 0.009850$. If all volume change is caused by dilatancy, then the dilatancy angle defined in terms of cumulative natural strain is $\psi = \sin^{-1}[\varepsilon_V/(\varepsilon_1 - \varepsilon_3)] \approx 2.814^\circ$. Our model does not compute strains, and instead estimates the continuously evolving dilatancy angle as $\psi = \tan^{-1}[\dot{\varepsilon}_V/\dot{\gamma}]$, where $\dot{\varepsilon}_V \equiv (1/V)(\mathrm{d}V/\mathrm{d}t) = -(1/m)(\mathrm{d}m/\mathrm{d}t)$ is the volumetric strain rate of the granular phase, and $\dot{\gamma} = 2\sqrt{\bar{u}^2 + \bar{v}^2}/h$ is the depth-averaged shear rate estimated from the local flow thickness h and depth-averaged velocity components $\bar{u}$ and $\bar{v}$. For the deformation increment depicted here, we find that $\dot{\varepsilon}_V \approx \int_{V_0}^{V_1} \mathrm{d}V/V\Delta t = \ln(V_1/V_0)/\Delta t = 0.009850/\Delta t$ and $\dot{\gamma} = 2\bar{u}/h \approx 0.2010/\Delta t$, which yields $\psi \approx 2.806^\circ$, a value that differs only slightly from the more-precisely calculated value noted above.

[55,62]. Therefore, the debris compressibility α can be defined by using a relationship commonly employed in soil mechanics [58]

$$\alpha = \frac{1}{m}\frac{\partial m}{\partial \sigma_e}. \tag{3.13}$$

This relationship may alternatively be expressed as $\alpha = [m(\rho_s - \rho_f)]^{-1}(\partial\rho/\partial\sigma_e)$, a form that reveals an analogy with ideal-gas compressibility. Just as compression of a gas can be a nearly reversible process, α can be regarded as a nearly reversible, elastic compressibility, because the pore volume change described by (3.13) arises largely from localized elastic shear straining of grain asperities that exist where irregular grains contact one another [55,67]. On the other hand, (3.13) implies that α cannot be a constant. Indeed, if α were constant and $\dot{\gamma} = 0$ were enforced, then (3.13) and (3.12) would lead to $\mathrm{d}m/\mathrm{d}t = m\alpha(\mathrm{d}\sigma_e/\mathrm{d}t)$, indicating that exponential growth of m would occur in response to any growth of σ_e.

Existing data provide guidance for evaluating variation of α as a function of m and σ_e. Gravity-driven consolidation of unconfined, nearly liquefied debris-flow slurries with $m \geq 0.4$ generally exhibits behaviour consistent with $\alpha \approx 10^{-5}\,\mathrm{Pa}^{-1}$ [61,68]. Compressibilities as large as $\alpha \sim 10^{-2}\,\mathrm{Pa}^{-1}$ have been measured for relatively dilute, mud-rich slurries and dredged sludges with $\sigma_e < 10^3$ Pa and $m < 0.4$ [69–71], whereas values $\alpha \sim 10^{-7}\,\mathrm{Pa}^{-1}$ are more typical of loosely packed sand and sand–gravel mixtures with $\sigma_e > 10^4$ Pa and $m > 0.55$ [72,73]. For virtually all soils and debris slurries, values of α increase monotonically as values of σ_e and m decrease (cf. [5,74]), although α must approach some upper limit when σ_e is sufficiently small. To reconcile these observations with (3.13), we postulate the constitutive relationship

$$\alpha = \frac{a}{m(\sigma_e + \sigma_0)}, \tag{3.14}$$

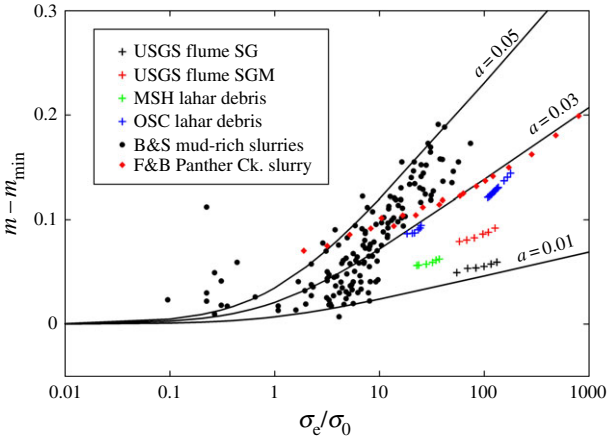

Figure 3. Graphs of equation (3.15) (solid lines) and data obtained in laboratory measurements of the compressibilities of six quasi-static debris mixtures. 'USGS flume SG' and 'USGS flume SGM' refer to sand–gravel and sand–gravel–mud mixtures used in large-scale debris-flow experiments of Iverson *et al.* [10]. 'MSH lahar debris' and 'OSC lahar debris' refer to mixtures reconstituted from deposits of two large debris flows: the North Fork Toutle lahar of 18 May 1980 at Mount St. Helens (MSH), USA [75], and the Osceola (OSC) lahar of about 5600 years ago at Mount Rainier, USA [76]. Data for all of the aforementioned materials were obtained from triaxial loading tests reported by Major [72]. 'B&S mud-rich slurries' refers to data reported by Been & Sills [69], and F&B Panther CK refers to data reported by Fox & Baxter [71]. Each of these studies involved slurries that were finer grained and more dilute than the materials studied by Major [72].

where a is a proportionality coefficient and σ_0 is a reference stress that establishes the maximum debris compressibility, $a/m\sigma_0$, which applies when $\sigma_e = 0$.

The implications of our constitutive relationship for α can be seen most clearly by combining (3.14) with (3.13) and (3.12), and then integrating the resulting equation for a special case with $\dot{\gamma} = 0$ or $\partial m/\partial \gamma = 0$ (i.e. zero shear rate or zero dilatancy). This operation yields the solution

$$m - m_{min} = a \ln \left[\frac{\sigma_e}{\sigma_0} + 1 \right], \tag{3.15}$$

which satisfies the auxiliary condition $m = m_{min}$ when $\sigma_e = 0$. Graphs of (3.15) can be compared with data obtained in laboratory compression and slurry-consolidation tests of diverse debris-like materials (figure 3). Because none of the tests involved gravity-free conditions in which an ideal limiting state with $m = m_{min}$ and $\sigma_e = 0$ was attained, we extrapolated the data for m as a function of σ_e in order to estimate the values of m_{min} and σ_0 necessary for normalizing the data in figure 3 (Table 1). Use of alternative values of m_{min} and σ_0 would not affect the slopes of the data trends depicted in the figure, however. These trends show that the most-plausible values of a in (3.15) range from about 0.01 to 0.05, irrespective of the debris composition. The largest values of a as well as the smallest values of $m_{min}$and σ_0 apply to mixtures with the highest mud contents. Owing to the ability of (3.15) to mimic the data trends in figure 3, we adopt (3.14) as our definition of debris compressibility, and we infer that values $0.01 \leq a \leq 0.05$ and $10\,\text{Pa} \leq \sigma_0 \leq 1000\,\text{Pa}$ in (3.14) are commonly suitable. Model predictions presented in our companion paper [46] help test the validity of this inference.

(f) Definition of dilatancy

The dilatancy of granular materials is traditionally expressed as an angle, as discussed in detail by Rowe [77], Nemat-Nasser [78], Bolton [23], Houlsby [24] and Rao & Nott [79]. In our model, evolving values of the dilatancy angle ψ are not specified. Instead they are the by-product

Table 1. Debris materials, data sources and data-normalization factors used to assemble figure 3.

material (and data source)	m_{min}	σ_0 (Pa)[a]
USGS debris flume SG mixture [72, appendix 1]	0.62	1000
USGS debris flume SGM (or SGL) mixture [72, appendix 1]	0.58	1000
MSH mixture from Mount St. Helens lahar [72, appendix 1]	0.60	1000
OSC mixture from Osceola lahar [72, appendix 1]	0.40	1000
B&S mud slurries [69, fig. 16]	0.06	10
F&B Panther Creek slurry [71, fig. 8]	0.10	100

[a]Tabulated values of σ_0 are order-of-magnitude estimates of the characteristic intergranular normal stress based on data reported for each set of experiments.

of coupled evolution of the solid volume fraction, flow velocity, flow thickness and pore-fluid pressure. Nevertheless, ψ can also be interpreted as a state-dependent material property defined by

$$\tan\psi = \frac{1}{V}\frac{\partial V}{\partial \gamma} = -\frac{1}{m}\frac{\partial m}{\partial \gamma}, \tag{3.16}$$

where, for a fixed mass of grains, $\partial V/V$ is the part of the natural volume strain caused by an increment of shear strain $\partial\gamma$ (figure 2). This definition of ψ is similar to that used in theories of quasi-static plastic deformation of rocks and soils [55], but our model avoids explicit evaluation of strains and instead combines (3.16) with (3.12) and (3.13) to recast the definition of ψ in terms of rates

$$\dot{\gamma}\tan\psi = \alpha\frac{\mathrm{d}\sigma_e}{\mathrm{d}t} - \frac{1}{m}\frac{\mathrm{d}m}{\mathrm{d}t}. \tag{3.17}$$

Thus, for any non-zero shear rate $\dot{\gamma}$, (3.17) describes how ψ is related to the total dilation rate $(-1/m)\mathrm{d}m/\mathrm{d}t$ and the portion of the total dilation rate caused by changes in the mean effective stress, $\alpha(\mathrm{d}\sigma_e/\mathrm{d}t)$.

Some key implications of (3.17) can be illustrated by considering special cases. For example, if $\alpha = 0$ or $\mathrm{d}\sigma_e/\mathrm{d}t = 0$, then (3.17) reduces to $\mathrm{d}m/\mathrm{d}t = -m\dot{\gamma}\tan\psi$, which indicates that unsustainable growth or decay of m would occur in the presence of constant ψ and $\dot{\gamma}$. Thus, values of ψ must evolve as values of σ_e and m evolve during deformation. For experiments in which steady values of $\dot{\gamma}$ and m are imposed, (3.17) implies that ψ evolves during a start-up phase in which σ_e evolves until $\mathrm{d}\sigma_e/\mathrm{d}t = 0$ and $\psi = 0$ are satisfied. This equilibration of σ_e to an imposed $\dot{\gamma}$ and m is tantamount to development of steady dispersive normal stress in the enclosed shear cell experiments of Bagnold [80] (cf. [81,82]). On the other hand, if a steadily shearing grain–fluid mixture freely dilates or contracts when a step change in σ_e is externally imposed, then (3.17) implies that $\dot{\gamma}$ subsequently equilibrates to a new steady state as $\mathrm{d}m/\mathrm{d}t \to 0$ and $\psi \to 0$. Boyer *et al.* [39] observed this type of equilibration in experiments more relevant than those of Bagnold [80]—at least with respect to gravity-driven geophysical flows—because Boyer *et al.* [39] employed a stress-controlled shear cell that allowed unrestricted evolution of m and attendant pore-fluid flow.

Although (3.17) is consistent conceptually with broad patterns of behaviour observed in experiments, it gives an incomplete description of dilatancy. It provides no relationship between instantaneous values of ψ, $\dot{\gamma}$, m and σ_e, and it contains no information about behaviour in the static limit $\dot{\gamma} \to 0$. No fundamental theory provides a framework for linking these quantities in diverse granular states [36,83], but Forterre & Pouliquen [25] present a variety of evidence indicating that, for dense granular flows, ψ can be viewed as a material property that depends on the evolving difference between the ambient solid volume fraction m and a volume fraction m_{eq} that is equilibrated to the ambient confining pressure and shear rate. Dilatancy can thereby exhibit memory effects as well as dependence on the instantaneous state of the material (cf. [84]).

This approach effectively extends concepts that were originally developed in critical-state models of quasi-static soils [22], and we employ it in our model.

To evaluate the instantaneous relationship between $\tan\psi$ and $m - m_{eq}$ in disequilibrium states, we adopt a linear formula used by Roux & Radjai [85] and Pailha & Pouliquen [38], who inferred that $\tan\psi = K(m - m_{eq})$, where K is a calibration factor. Moreover, to limit the number of adjustable parameters in our model, we tentatively set $K = 1$, and thereby define

$$\tan\psi = m - m_{eq}. \tag{3.18}$$

This relationship implies that ψ generally falls in the range $-0.2 < \psi < 0.2$ (radians) in our model, because debris-flow materials typically have $0.4 \leq m \leq 0.8$ and $m_{eq} \approx 0.6$.

To gauge the combined effects of the stress state and shear rate on m_{eq}, we use a dimensionless parameter similar to the 'viscous number' $I_v = \mu\dot{\gamma}/\sigma_e$ used by Pailha & Pouliquen [38] and Boyer *et al.* [39] (cf. [86,87]). However, because our model allows for the development of fully liquefied states with $\sigma_e = 0$, we use a generalized dimensionless parameter, N, which has a value that remains finite in such states

$$N = \frac{\mu\dot{\gamma}}{\rho_s\dot{\gamma}^2\delta^2 + \sigma_e}. \tag{3.19}$$

Here, μ is the effective shear viscosity of muddy pore fluid, and δ is a length scale associated with generation of normal stresses by grain collisions during shearing (cf. [80,88]). For flows of geological debris containing a great diversity of grains, the value of δ is not well constrained. Therefore, in our model we simply set $\delta = 0.001$ m to match the size of typical sand grains.

Physical interpretation of N is facilitated by noting that (3.19) can be recast as

$$N = \frac{I_v}{I_v S + 1}, \tag{3.20}$$

where S is a Stokes number defined as $S = (\rho_s\dot{\gamma}\delta^2)/\mu$. For typical debris-flow conditions in which the values $\rho_s = 2700\,\mathrm{kg\,m^{-3}}$, $0 < \dot{\gamma} \leq 10\,\mathrm{s^{-1}}$, $\delta = 0.001$ m, $0.001 \leq \mu \leq 0.1$ Pa-s and $10 \leq \sigma_e \leq 10^6$ Pa apply, the values $0 \leq I_v \leq 0.1$ and $0 < S < 30$ apply in (3.20). These values indicate that the full range of typical N values is $0 \leq N \leq 0.1$, and that the range of N commonly mirrors that of I_v. The only significant difference in the values of N and I_v arises if $\sigma_e < 10$ Pa, in which case $N \to 1/S$ as $\sigma_e \to 0$ and $I_v \to \infty$. Therefore, in our model, $N = 1/S$ is an upper bound value that applies if grain motion is almost fully damped by fluid viscosity. (The mathematical singularity at $S = 0$ is physically irrelevant unless there is perfect damping, which cannot occur in moving debris described by our model.)

The function $m_{eq}(N)$ can be inferred from experimental data and from physical constraints that imply behavioural limits. In the static limit with $I_v = 0$ and $N = 0$, the value $m_{eq} = m_{crit}$ applies, where m_{crit} is the critical-state volume fraction defined for lithostatically stressed states in normally consolidated soils [22]. Few direct measurements of m_{crit} for poorly sorted geological debris exist, but limited data indicate that a reasonable range is $0.5 \leq m_{crit} \leq 0.7$ [16]. The relationship between m_{crit}, m_{eq} and I_v for non-static cases has been revealed most clearly by Boyer *et al.* [39], who found that the function

$$m_{eq}(I_v) = \frac{m_{crit}}{1 + \sqrt{I_v}} \tag{3.21}$$

provided an excellent fit to experimental data for various mixtures of liquids and uniform spheres that were incompletely liquefied. In lieu of similarly detailed information for debris mixtures that contain diverse grains, we combine the approximation $N \approx I_v$ with (3.21) with (3.18) to pose what we believe is the simplest plausible constitutive relationship for state-dependent debris-flow dilatancy

$$\tan\psi = m - \frac{m_{crit}}{1 + \sqrt{N}}. \tag{3.22}$$

Taken together, (3.17) through (3.22) imply that disequilibrium values of m tend to relax towards an equilibrium value m_{eq} that depends on N. If $N = 0$, then $m_{eq} = m_{crit}$ applies. The relaxation

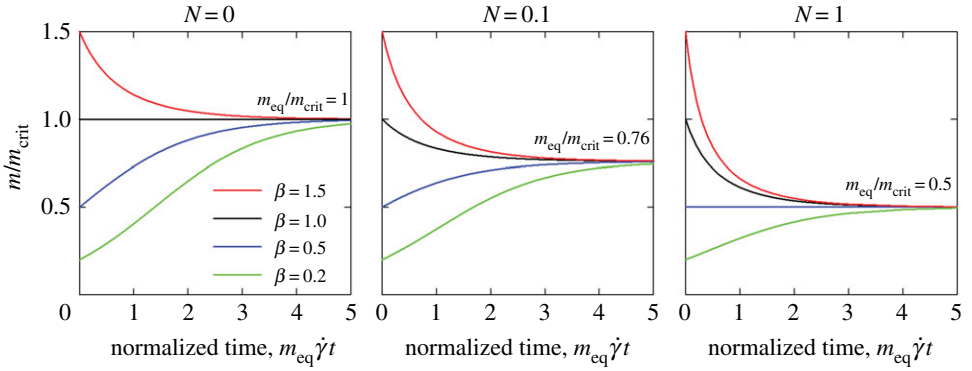

Figure 4. Graphs of equation (3.24), illustrating relaxation behaviour of m for cases in which N has the constant values 0, 0.1 or 1. The initial condition is $m(0)/m_{crit} = \beta$. For N=0, m relaxes to m_{crit}. For $N > 0$, m relaxes to a dynamic equilibrium value m_{eq} that is smaller than m_{crit}.

time for m can be evaluated precisely for a special case in which $\dot{\gamma}$, σ_e and N are constants [38]. In this case, combination of (3.17) and (3.22) yields

$$\frac{dm}{dt} = \dot{\gamma} m \left[\frac{m_{crit}}{1 + \sqrt{N}} - m \right], \tag{3.23}$$

in which $m_{crit}/(1 + \sqrt{N})$ is constant. A useful solution of (3.23) satisfies the initial condition $m(0) = \beta m_{crit}$, where $\beta > 1$ describes initial states denser than the static critical state, and $\beta < 1$ describes initial states looser than the static critical state. This solution

$$\frac{m}{m_{crit}} = \left[1 + \sqrt{N} - \left(1 + \sqrt{N} - \frac{1}{\beta} \right) \exp(-m_{eq} \dot{\gamma} t) \right]^{-1} \tag{3.24}$$

indicates that m approaches m_{eq} in a manner that depends on both β and N, but in every case the approach occurs with a characteristic relaxation time $1/m_{eq}\dot{\gamma}$ (figure 4). Because mature debris flows typically have m_{eq} values of roughly 0.6 and $\dot{\gamma}$ values larger than $1\,s^{-1}$ [5], (3.24) implies that the relaxation $m \rightarrow m_{eq}$ typically would occur in less than 2 s if N were constant and no pore fluid were present. However, in our model relaxation of m is strongly regulated by evolution of pore-fluid pressure, as described below.

(g) Definition of pore-fluid viscosity and solid–fluid drag

On the basis of diverse evidence summarized by Iverson [5], we define the debris-flow fluid phase as water plus persistently suspended clay and silt-sized particles (collectively called mud particles) with effective diameters smaller than about 62 μm. In most natural debris flows and in large-scale experiments, the mud suspension has inferred solid volume fractions less than 0.2 [10,57]. These relatively dilute mud suspensions generally have effective viscosities that exceed that of pure water (approx. 0.001 Pa-s) by a factor ranging from about 5 to 100, whereas suspensions with solid volume fractions >0.4 can have viscosities that exceed that of water by a factor more than 1000 [3,89]. Furthermore, as the mud volume fraction increases, nonlinear rheological effects become increasingly prominent, particularly if mud particles consist of colloidal or chemically reactive clay [4,90,91]. Here, for the sake of parsimony, we neglect possible nonlinearities and treat pore fluid as an incompressible, Newtonian viscous material with a constant shear viscosity μ. Moreover, we assume that on a bulk scale, the liquid's shear deformation rate can be represented adequately by a deformation-rate tensor R that applies to

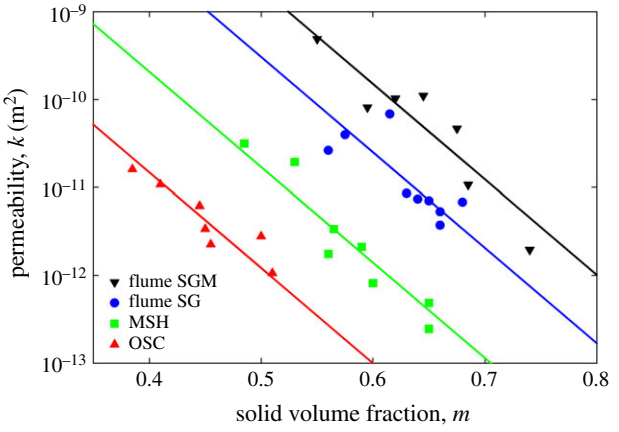

Figure 5. Data from compaction permeameter tests of diverse debris mixtures (adapted from [5,72]). 'Flume SGM' and 'Flume SG' denote standard mixtures used in the large-scale debris-flow experiments of Iverson *et al.* [10]. 'MSH' and 'OSC' denote mixtures extracted from deposits of two large debris flows: the North Fork Toutle flow of 18 May 1980 at Mount St Helens (MSH), USA [75], and the Osceola flow (OSC) of about 5600 years ago at Mount Rainier, USA [76]. For the MSH and OSC mixtures, only grains smaller than 16 mm were included in tests. Lines depict graphs of equation (3.27) fitted to data by using the values $k_0 = 1.5 \times 10^{-10}$ m^2 for Flume SG, $k_0 = 2.5 \times 10^{-11}$ m^2 for Flume SGM, $k_0 = 1.4 \times 10^{-12}$ m^2 for MSH and $k_0 = 1.0 \times 10^{-13}$ m^2 for OSC.

the solid–fluid mixture as a whole. We therefore use the fluid-phase constitutive equation [50]

$$T_{\text{vis}} = 2\mu R. \tag{3.25}$$

Pore-fluid viscosity influences debris-flow behaviour not only by dissipating energy during bulk shearing, but also by exerting drag as fluid moves with respect to adjacent solid grains. Because grain sizes and shapes in geological debris are very diverse, drag formulae for specific grain sizes and shapes have limited applicability. As an alternative, we treat drag as a bulk continuum phenomenon that reflects the influences of solid–fluid interactions integrated over the entire grain-size distribution. For this purpose, we use Darcy's Law

$$\boldsymbol{q} = -\frac{k(m)}{\mu}\nabla p_{\text{e}}, \tag{3.26}$$

where $k(m)$ is the hydraulic permeability of the granular aggregate, and p_{e} is the excess pore-fluid pressure defined in (3.9). For the function $k(m)$, we use the empirical formula

$$k(m) = k_0 \exp\left(\frac{0.6 - m}{0.04}\right), \tag{3.27}$$

which provides acceptable fits to data obtained from compaction permeameter testing of quasi-static debris with compositions that span much of the range observed in nature (figure 5). For this broad spectrum of debris, the reference permeability k_0 in (3.27) has values that range from about 10^{-10} m^2 for debris with approx. 2% mud content to 10^{-13} m^2 for debris with about 50% mud content by dry weight. Large volumes of rapidly shearing debris are probably characterized by larger values of k_0 owing to the effects of agitation that opens transient pathways for fluid flow, and also to the effect of scale on the effective permeabilities of porous media [92]. However, no measurements have been performed on large volumes of agitated, poorly sorted debris. Therefore, we infer that k_0 may have values larger (but not smaller) than those portrayed in figure 5.

Because values of k are probably no larger than about 10^{-7} m^2 in realistic, agitated debris, and because values of μ in muddy pore water are about $10^{-2} - 10^{-1}$ Pa-s, we infer that the

excess pore-pressure gradients described by (3.25) can readily have magnitudes comparable to those of hydrostatic gradients ($\nabla p_e \sim \rho_f g \sim 10^4\,\mathrm{Pa\,m^{-1}}$). Gradients of at least this size occur if the magnitude of $\boldsymbol{q}$ exceeds $10^{-1}\,\mathrm{m\,s^{-1}}$ in debris-flow materials with the largest k/μ values and if it exceeds $10^{-8}\,\mathrm{m\,s^{-1}}$ in debris-flow materials with the smallest k/μ values. Development of excess pore-pressure gradients can inhibit debris dilation and contraction, and these gradients serve as a volume-averaged surrogate for the effects of local lubrication forces where individual grains displace fluid in adjacent pores [90,93,94]. In turn, inhibition of dilation or contraction produces feedbacks that can lead to regulation of ∇p_e by diffusive redistribution of excess pore-fluid pressure.

(h) Diffusive redistribution of excess pore-fluid pressure

The relationship between the excess pore-pressure gradient described by (3.26) and the dilation rate described by (3.17) implies that pore-pressure evolution is mathematically analogous to forced diffusion (cf. [95]). This analogy can be established by first combining (3.10), (3.11) and (3.26) to find that

$$\frac{1}{m}\frac{\mathrm{d}m}{\mathrm{d}t} = -\nabla\cdot\left[\frac{k}{\mu}\nabla p_e\right]. \tag{3.28}$$

The volume fraction m can be eliminated from (3.28) by combining it with (3.17) to obtain

$$\frac{\mathrm{d}\sigma_e}{\mathrm{d}t} = -\frac{k}{\alpha\mu}\nabla^2 p_e - \frac{1}{\alpha}\left[\nabla\frac{k}{\mu}\right]\cdot\nabla p_e + \frac{\dot{\gamma}\tan\psi}{\alpha}, \tag{3.29}$$

where $k/\alpha\mu$ plays the role of a pore-pressure diffusivity. Finally, definitions (3.8) and (3.9) can be used to infer that $\mathrm{d}\sigma_e/\mathrm{d}t = \mathrm{d}\sigma/\mathrm{d}t - \mathrm{d}p_e/\mathrm{d}t - \mathrm{d}p_h/\mathrm{d}t$, and substitution of this relationship in (3.29) enables the equation to be recast as a forced, advection–diffusion equation for p_e,

$$\frac{\mathrm{d}p_e}{\mathrm{d}t} - \frac{k}{\alpha\mu}\nabla^2 p_e - \frac{1}{\alpha}\left[\nabla\frac{k}{\mu}\right]\cdot\nabla p_e = \frac{\mathrm{d}(\sigma - p_h)}{\mathrm{d}t} - \frac{\dot{\gamma}\tan\psi}{\alpha}, \tag{3.30}$$

where, as above, $\mathrm{d}/\mathrm{d}t = \partial/\partial t + \boldsymbol{v}_s\cdot\nabla$. If all time derivatives are zero and $\dot{\gamma}\tan\psi$ is constant, then (3.30) reduces to the steady-state balance $\nabla\cdot[(k/\mu)\nabla p_e] = \dot{\gamma}\tan\psi$, which can alternatively be expressed as $-\nabla\cdot\boldsymbol{q} = \dot{\gamma}\tan\psi$. This result shows that porosity creation during steady dilation is balanced by a steady influx of fluid that fills the enlarging pores.

The forcing effects described by the right-hand side of (3.30) can drive rapid pore-pressure change, but p_e can also evolve in the absence of forcing owing to diffusion described by the left-hand side of (3.30). A standard diffusion-equation normalization shows that p_e relaxes diffusively with a time-scale $h^2\alpha\mu/k$, where h is the debris-flow thickness (i.e. the distance over which pore-pressure diffusion typically occurs). For the range of k/μ values considered above ($10^{-12} - 10^{-5}\,\mathrm{m^3\,kg^{-1}\,s}$) and the representative value $\alpha = 10^{-5}\,\mathrm{Pa^{-1}}$, $h = 1\,\mathrm{m}$ implies that timescales of unforced pore-pressure diffusion can range from roughly 1 s to 30 years. Thus, in an extreme case involving flow of gravel and water with little finer sediment, excess pore pressure may dissipate diffusively on a timescale much shorter than that of a flow duration. In the opposite extreme (e.g. a large, clay-rich volcanic debris flow), pore-pressure dissipation may proceed so slowly that its effects are modest until long after downstream motion has ceased. As a result of the dependence of the diffusion timescale on h^2, large debris flows can readily maintain higher fluid pressures, lower Coulomb friction, and greater mobility than can small flows with the same composition [5].

(i) Coulomb friction

An abundance of evidence indicates that Coulomb friction generates most of the resistance to debris-flow motion—particularly if Coulomb behaviour is defined as a proportionality between shear stresses and normal stresses on planes of shearing, irrespective of the shear rate [11]. With this definition, Coulomb friction characterizes the shear-to-normal stress ratio in most quasi-static

soils [96], in dense granular flows with enduring grain contacts [25], in more dilute granular flows characterized by brief grain collisions [97], and in shear flows of concentrated solid–liquid mixtures [39,80]. Indeed, on a bulk continuum scale, a proportionality between normal and shear stresses on planes of shearing appears to be a nearly universal property of granular materials.

In our model, the Coulomb friction rule represents the influences not only of grain-boundary friction but also of dilatancy and modification of normal stresses at grain contacts by pore-fluid pressure. On the basis of well-established principles of soil mechanics and empirical evidence [98,99], we use the effective stress T_e defined in (3.7) as the stress that influences bulk frictional resistance to shearing. Thus, if all else is constant, frictional resistance decreases as pore pressure locally increases. Dilatancy ψ influences bulk shear resistance through geometrical effects on grain rearrangement. Following the rationale of Rowe [77], Nemat-Nasser [78], Bolton [23] and Houlsby [24], we infer that the effects of ψ contribute additively to those of a constant-volume friction angle ϕ, which characterizes friction under conditions with $m = m_{eq}$. By embedding this effect of ψ and also embedding the effect of pore pressure, we express the Coulomb friction rule as

$$\boldsymbol{\tau}_s = \frac{\boldsymbol{v}}{\|\boldsymbol{v}\|}[(\sigma_n - p)\tan(\phi + \psi)], \tag{3.31}$$

where $\boldsymbol{\tau}_s$ is the granular-phase shear stress vector acting on planes of shearing, σ_n is the total normal stress on these planes, and $\boldsymbol{v}/\|\boldsymbol{v}\|$ indicates that positive shear stresses resist motion. The Coulomb rule can be expressed more completely in three-dimensional tensor form [100], but this complication is unnecessary here because we do not evaluate three-dimensional stress states in our depth-averaged model. A further complication is that Coulomb friction may exhibit rate-dependence, manifested as a gradual increase of ϕ as a function of I_v [39]. Here, for the sake of parsimony, we neglect this effect, although (3.31) implies that granular shear resistance exhibits some implicit rate-dependence owing to the effects of the shear rate on ψ and p.

4. Depth-averaged model equations

Our depth-averaged model describes coupled evolution of the flow thickness $h(x, y, t)$, solid volume fraction $m(x, y, t)$, basal pore-fluid pressure $p_b(x, y, t)$ and depth-averaged components of the mixture velocity, which are $\bar{u}(x, y, t)$ in the x-direction and $\bar{v}(x, y, t)$ in the y-direction. The z component of the mixture velocity, w, is not predicted explicitly, but it is related to h, $u(h)$ and $v(h)$ through the kinematic boundary conditions

$$w(h) = \frac{\partial h}{\partial t} + u(h)\frac{\partial h}{\partial x} + v(h)\frac{\partial h}{\partial y}, \quad w(0) = 0, \tag{4.1}$$

which apply at $z = h(x, y, t)$ and at a rigid basal boundary, where $z = 0$.

The necessity of specifying the direction of depth integration *a priori* makes the choice of a coordinate system crucial. Some depth-averaged models use an Earth-centred, orthogonal Cartesian coordinate system with z vertical, which has the advantage of being independent of terrain geometry. This approach leads to complicated mechanical considerations when accounting for the effects of steep, irregular topography, however [101]. Other models, including the one we present here, use a z-coordinate normal to the local ground surface, such that the x-coordinate is directed downslope and the y-coordinate is directed cross-slope (figure 6). This approach, also, has limitations, because curvilinear coordinates are needed to adapt it to irregular terrain, limiting the utility of conventional digital elevation models of Earth's topography. Here, to emphasize the main new features of our model, we omit the effects of bed curvature and focus on flows that traverse planar terrain. Our companion paper [46] addresses bed curvature effects.

(a) Mass balances

Our model includes two mass-balance equations: one for the solid–fluid mixture as a whole and one for the granular solid phase. Because no data exist that document variations of the bulk density ρ or solid volume fraction m as a function of z in realistic debris flows, the equations

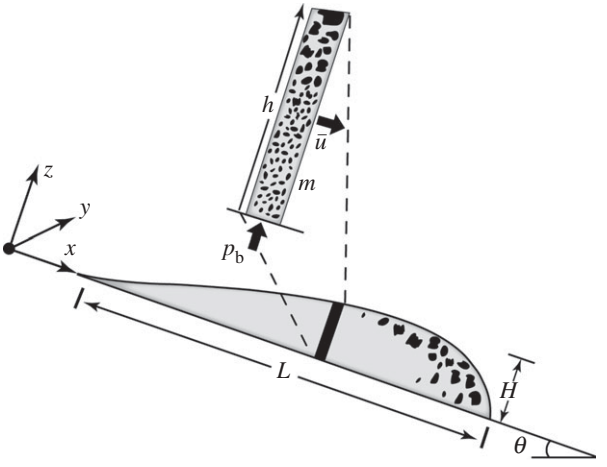

Figure 6. Schematic vertical cross-sectional view of a debris flow descending a planar slope inclined at the angle θ. The coordinate system and flow length scales H and L are defined. Magnified slice illustrates four of the dependent variables used in the depth-averaged model: $\bar{u}$, h, basal pore pressure p_b and solid volume fraction m. An additional dependent variable, not illustrated here, is the depth-averaged velocity component in the y-direction, $\bar{v}$.

assume that $\rho(x,y,t)$ and $m(x,y,t)$ are uniform at all depths below the surface at $z=h(x,y,t)$. However, the definition of h itself involves a potential ambiguity: because rocks may protrude variable distances above the adjacent liquid at the surface of debris flows, solid and liquid volume fractions may be ill defined in the vicinity. To avoid this ambiguity, we define $z=h(x,y,t)$ as the position of a *virtual* free surface, such that the debris-flow mass per unit basal area $\Delta x\Delta y$ is given by $\rho h(x,y,t)$ (figure 7). In effect, this definition replaces some combination of solid or liquid mass immediately above or below $h(x,y,t)$ with a thin, equivalently massive, homogeneous layer with a density ρ and upper surface at $h(x,y,t)$. In this way, $\rho h(x,y,t)$ is conserved, despite the fact that solid or liquid constituents may pass through $h(x,y,t)$ during dilation or contraction.

The depth-integrated dilation rate $D(x,y,t)$ plays a key role in our mass-balance equations. It is defined by integrating (3.10) through the flow thickness to obtain

$$D(x,y,t)\equiv\int_0^h(\nabla\cdot\boldsymbol{v}_s)\mathrm{d}z=-\int_0^h\frac{1}{m}\frac{\mathrm{d}m}{\mathrm{d}t}\mathrm{d}z=-\frac{h}{m}\frac{\bar{\mathrm{d}}m}{\bar{\mathrm{d}}t}. \tag{4.2}$$

Here and in subsequent equations $\bar{\mathrm{d}}/\bar{\mathrm{d}}t=\partial/\partial t+\bar{u}\partial/\partial x+\bar{v}\partial/\partial y$ denotes a depth-averaged material time derivative. Expansion of $\bar{\mathrm{d}}m/\bar{\mathrm{d}}t$ in (4.2) leads to a primitive depth-integrated evolution equation for the solid volume fraction

$$\frac{\partial m}{\partial t}+\bar{u}\frac{\partial m}{\partial x}+\bar{v}\frac{\partial m}{\partial y}=-\frac{Dm}{h}, \tag{4.3}$$

in which the source term $-Dm/h$ accounts for the effects of dilation or contraction on m.

A depth-averaged mass-conservation equation that describes evolution of ρh for the solid–fluid mixture as a whole results from integrating (3.1) using Leibniz' rule and the kinematic boundary conditions (4.1) to find that

$$\begin{aligned}\int_0^h\left(\frac{\partial\rho}{\partial t}+\nabla\cdot\rho\boldsymbol{v}\right)\mathrm{d}z&\\ =\rho\left[\frac{\partial(h\bar{u})}{\partial x}-u(h)\frac{\partial h}{\partial x}+\frac{\partial(h\bar{v})}{\partial y}-v(h)\frac{\partial h}{\partial y}+w(h)-w(0)\right]+h\frac{\bar{\mathrm{d}}\rho}{\bar{\mathrm{d}}t}&\\ =\rho\left[\frac{\partial h}{\partial t}+\frac{\partial(h\bar{u})}{\partial x}+\frac{\partial(h\bar{v})}{\partial y}\right]+h\frac{\bar{\mathrm{d}}\rho}{\bar{\mathrm{d}}t}=0.&\end{aligned} \tag{4.4}$$

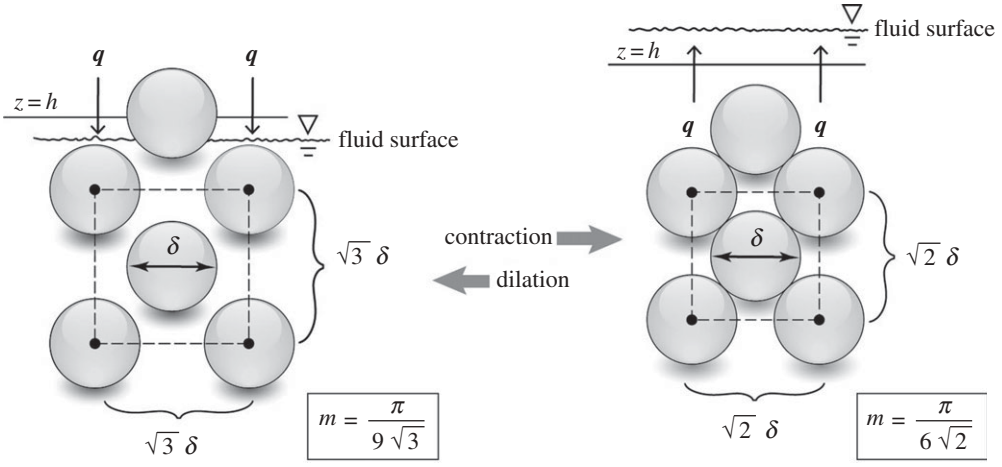

Figure 7. Schematic of the change in the position of the virtual free surface at $z = h$ in response to dilation or contraction of a mixture with $\rho_s/\rho_f = 2.7$. Dashed lines indicate two-dimensional boundaries of isometric three-dimensional unit cells used to calculate the solid volume fraction, m. For illustrative purposes, solid grains are assumed to be identical spheres with diameter δ, and sphere centre spacings are chosen as either $\sqrt{3}\delta$ or $\sqrt{2}\delta$. Spheres do not contact one another in either the dilated or contracted state illustrated here. A flux of pore fluid ($\boldsymbol{q}$) through the virtual free surface at $z=h$ accompanies changes in m caused by dilation or contraction. The idealized geometries used in this illustration exaggerate changes in m, $\boldsymbol{q}$ and h relative to changes that would occur in debris-flow materials containing grains with diverse shapes and sizes.

The term $h(\bar{\mathrm{d}}\rho/\bar{\mathrm{d}}t)$ can be recast by using the definition $\rho = \rho_s m + \rho_f(1 - m)$ in conjunction with (4.3) to obtain

$$h\frac{\bar{\mathrm{d}}\rho}{\bar{\mathrm{d}}t} = -(\rho - \rho_f)D. \tag{4.5}$$

Substituting (4.5) into (4.4) yields the equation we use to describe depth-averaged mass conservation of the solid–fluid mixture

$$\frac{\partial h}{\partial t} + \frac{\partial(h\bar{u})}{\partial x} + \frac{\partial(h\bar{v})}{\partial y} = \frac{\rho - \rho_f}{\rho}D. \tag{4.6}$$

Interpretation of the source term in (4.6) is straightforward for special cases with $\rho_f = 0$ (which implies that ρ and h describe attributes of only a granular phase) or with $\rho_f = \rho$ (which implies that ρ and h are uninfluenced by dilation or contraction because the debris effectively behaves as a homogeneous, incompressible material). In the more-general case with $0 < \rho_f < \rho$, $(\rho - \rho_f)D$ describes the simultaneous effects of a source ρD and sink $-\rho_f D$ as fluid mass replaces solid mass in dilating debris beneath h. In this case, the surface $h(x, y, t)$ coincides with neither the fluid surface nor the solid surface, but rather with that of the virtual free surface described above (figure 7).

Use of (4.6) also enables (4.3) to be recast in a form that accounts for simultaneous evolution of m and h. Multiplication of (4.6) by m and multiplication of (4.3) by h, followed by addition of the resulting equations, yields the depth-averaged equation we use to evaluate evolution of the solid volume fraction

$$\frac{\partial(hm)}{\partial t} + \frac{\partial(h\bar{u}m)}{\partial x} + \frac{\partial(h\bar{v}m)}{\partial y} = -\frac{\rho_f}{\rho}Dm. \tag{4.7}$$

An analogous equation can be obtained for the fluid volume fraction

$$\frac{\partial[h(1-m)]}{\partial t} + \frac{\partial[h\bar{u}(1-m)]}{\partial x} + \frac{\partial[h\bar{v}(1-m)]}{\partial y} = \frac{\rho_s}{\rho}Dm, \tag{4.8}$$

and addition of (4.7) and (4.8) reproduces (4.6). Thus, if (4.6) and (4.7) are satisfied, then (4.8) is satisfied as well.

The presence of finite source terms in (3.7) and (3.8), even for the special case with $\rho_s = \rho_f = \rho$, reflects the fact that $\rho_s hm$ and $\rho_f h(1-m)$ are not conserved beneath the virtual free surface at $z = h(x, y, t)$. Rather, ρh is the quantity conserved beneath this surface, and $\rho h = \rho_s hm$ or $\rho h = \rho_f h(1-m)$ are valid only if $\rho_f = 0$ or $\rho_s = 0$, respectively.

(b) Momentum balances

Depth-integrated equations for conservation of the x, y and z components of linear momentum are exactly analogous to one another. Therefore, we illustrate integration of only the x component, which is accomplished by using (3.2) and Leibniz' rule to obtain the left-hand side terms

$$\begin{aligned}
&\int_0^h \left[\frac{\partial(\rho u)}{\partial t} + \frac{\partial(\rho u^2)}{\partial x} + \frac{\partial(\rho uv)}{\partial y} + \frac{\partial(\rho uw)}{\partial z} \right] \mathrm{d}z \\
&= \frac{\partial(\rho h\bar{u})}{\partial t} - \rho u(h)\frac{\partial h}{\partial t} + \frac{\partial(\rho h\bar{u}^2)}{\partial x} - \rho u^2(h)\frac{\partial h}{\partial x} + \frac{\partial(\rho h\bar{u}\,\bar{v})}{\partial y} - \rho u(h)v(h)\frac{\partial h}{\partial y} + \rho u(h)\,w(h) - \rho u(0)w(0) \\
&= \rho\left[\frac{\partial(h\bar{u})}{\partial t} + \frac{\partial(h\bar{u}^2)}{\partial x} + \frac{\partial(h\bar{u}\,\bar{v})}{\partial y} \right] + h\bar{u}\frac{\bar{\mathrm{d}}\rho}{\bar{\mathrm{d}}t} \\
&= \rho\left[\frac{\partial(h\bar{u})}{\partial t} + \frac{\partial(h\bar{u}^2)}{\partial x} + \frac{\partial(h\bar{u}\,\bar{v})}{\partial y} \right] - (\rho - \rho_f)D\bar{u}. \qquad (4.9)
\end{aligned}$$

In the second line of (4.9), the second, fourth, sixth, seventh and eighth terms cancel one another through use of the kinematic boundary conditions (4.1). The third line of (4.9) results from rearrangement of the remaining terms, and the fourth line of (4.9) results from employing (4.5) to obtain the term $-(\rho - \rho_f)D\bar{u}$. This term describes a flux of x-momentum through the virtual free surface at $h(x, y, t)$ in response to dilation or contraction, but it does not imply that momentum enters or leaves the debris flow. Rather, the term reflects the fact that momentum is not conserved beneath $h(x, y, t)$ unless $D = 0$ or $\rho_f = \rho_s = \rho$. Although (4.9) can be written in alternative forms that lack D, we use the last line of (4.9) to illustrate the role of D and to clarify the relationship between our equations and standard, depth-integrated momentum equations for flows of incompressible material.

Depth integration of the x component of the right-hand side of (3.2) using Leibniz' rule yields

$$\int_0^h \left[\rho g_x - \frac{\partial \tau_{xx}}{\partial x} + \frac{\partial \tau_{yx}}{\partial y} + \frac{\partial \tau_{zx}}{\partial z} \right] \mathrm{d}z = \rho g_x h - \frac{\partial(\bar{\tau}_{xx}h)}{\partial x} + \frac{\partial(\bar{\tau}_{yx}h)}{\partial y} - \tau_{zx}(0), \qquad (4.10)$$

where g_x is the x component of $\boldsymbol{g}$, and $\bar{\tau}_{xx}$ and $\bar{\tau}_{yx}$ denote depth-averaged stress components. (Recall that we define τ_{xx} and other normal stress components as positive in compression). Except for the resisting basal shear traction $\tau_{zx}(0)$, all boundary terms introduced during depth integration vanish from (4.10), because we assume a traction-free upper boundary at $z = h$ and rigid basal boundary at $z = 0$.

Substitution of (3.9) and (4.9) into (3.2) yields the depth-averaged x-component momentum-conservation equation

$$\rho\left[\frac{\partial(h\bar{u})}{\partial t} + \frac{\partial(h\bar{u}^2)}{\partial x} + \frac{\partial(h\bar{u}\,\bar{v})}{\partial y} \right] - (\rho - \rho_f)D\bar{u} = \rho g_x h - \frac{\partial(\bar{\tau}_{xx}h)}{\partial x} + \frac{\partial(\bar{\tau}_{yx}h)}{\partial y} - \tau_{zx}(0). \qquad (4.11)$$

The depth-averaged y-component momentum equation is obtained by interchanging $\bar{u}$ and $\bar{v}$ as well as x and y in (4.11), yielding

$$\rho\left[\frac{\partial(h\bar{v})}{\partial t} + \frac{\partial(h\bar{v}^2)}{\partial y} + \frac{\partial(h\bar{v}\,\bar{u})}{\partial x} \right] - (\rho - \rho_f)D\bar{v} = \rho g_y h - \frac{\partial(\bar{\tau}_{yy}h)}{\partial y} + \frac{\partial(\bar{\tau}_{xy}h)}{\partial x} - \tau_{zy}(0). \qquad (4.12)$$

The depth-averaged z-momentum equation can be written in an Eulerian form analogous to that of (4.11) and (4.12), but it is useful to manipulate its left-hand side by employing (4.6) to obtain

the Lagrangian form

$$\rho h\frac{\bar{\mathrm{d}}\bar{w}}{\bar{\mathrm{d}}t}=\rho g_z h+\frac{\partial(\bar{\tau}_{xz}h)}{\partial x}+\frac{\partial(\bar{\tau}_{yz}h)}{\partial y}+\tau_{zz}(0), \tag{4.13}$$

in which $-(\rho-\rho_\mathrm{f})D\bar{w}$ has been incorporated into $\rho h(\bar{\mathrm{d}}\bar{w}/\bar{\mathrm{d}}t)$.

If shallow-flow scaling (detailed in §5) is used to justify neglect of $\partial(\bar{\tau}_{xz}h)/\partial x+\partial(\bar{\tau}_{yz}h)/\partial y$ in (4.13), then the equation reduces to a balance between the basal normal traction and the z component of the effective weight per unit area of the moving debris, $\rho g_z' h$ [101]

$$\tau_{zz}(0)=\rho g_z' h,\quad \text{where } g_z'=-g_z+\frac{\bar{\mathrm{d}}\bar{w}}{\bar{\mathrm{d}}t}. \tag{4.14}$$

Because z is reckoned positive upward (such that $g_z<0$), a positive acceleration ($\bar{\mathrm{d}}\bar{w}/\bar{\mathrm{d}}t>0$) adds to the effects of $-g_z$ and thereby increases the effective weight of the debris and the basal normal traction $\tau_{zz}(0)$. Lack of precise accounting for the effects of $\bar{\mathrm{d}}\bar{w}/\bar{\mathrm{d}}t$ is a fundamental limitation of depth-averaged flow models, including ours. Here, in order to focus on the key new features of our model, we employ the simplifying assumption $\bar{\mathrm{d}}\bar{w}/\bar{\mathrm{d}}t=0$, so that (3.13) reduces to

$$\tau_{zz}(0)=-\rho g_z h=\rho g h\cos\theta, \tag{4.15}$$

where θ is bed slope angle (figure 6), g is the magnitude of $\boldsymbol{g}$ and $g\cos\theta=-g_z$. In our companion paper [46], we describe our method of accounting for the effects of spatial variations in θ on flow dynamics.

(c) Basal pore pressure

We use depth integration and rational approximations to obtain a reduced pore-pressure evolution equation that contains the basal pore pressure p_b rather than p_e. The first step entails recasting (3.30) in terms of the total pore-fluid pressure, $p=p_\mathrm{e}+p_\mathrm{h}$, where $p_\mathrm{h}=\rho_\mathrm{f}g_z(h-z)$ is the hydrostatic pressure that balances the fluid weight. Next, we invoke shallow-flow scaling that applies if $H/L\ll 1$ (see §5), where H is the characteristic thickness and L is the characteristic length of a debris-flow surge (figure 6). This scaling indicates that $\partial^2p/\partial z^2\gg\partial^2p/\partial x^2$, $\partial^2p/\partial y^2$ because $\partial^2/\partial z^2$ scales with $1/H^2$, whereas $\partial^2/\partial x^2$ and $\partial^2/\partial y^2$ scale with $1/L^2$. Analogous reasoning indicates that $\partial/\partial x$, $\partial/\partial y\sim 1/L$ and $\partial/\partial z\sim 1/H$. Using these scales to identify and neglect terms of order H/L or smaller in (3.30) yields the reduced equation

$$\frac{\mathrm{d}p}{\mathrm{d}t}-\frac{k}{\alpha\mu}\frac{\partial^2p}{\partial z^2}-\frac{1}{\alpha}\frac{\partial(k/\mu)}{\partial z}\frac{\partial p}{\partial z}=\frac{\mathrm{d}\sigma}{\mathrm{d}t}-\frac{\dot{\gamma}\tan\psi}{\alpha}. \tag{4.16}$$

Another step involves use of the approximations $w\approx(z/h)\mathrm{d}h/\mathrm{d}t$, $u\approx\bar{u}$ and $v\approx\bar{v}$ to recast the total time derivatives in (4.16) as $\mathrm{d}/\mathrm{d}t=\bar{\mathrm{d}}/\bar{\mathrm{d}}t+(z/h)(\bar{\mathrm{d}}h/\bar{\mathrm{d}}t)\partial/\partial z$ (cf. [28]). We make this substitution and also the substitution $\partial(k/\mu)/\partial z=0$ (because we assume that no material property varies as a function of z), and thereby reduce (4.16) to

$$\frac{\bar{\mathrm{d}}p}{\bar{\mathrm{d}}t}-\frac{k}{\alpha\mu}\frac{\partial^2p}{\partial z^2}=\frac{\bar{\mathrm{d}}\sigma}{\bar{\mathrm{d}}t}+\frac{z}{h}\frac{\bar{\mathrm{d}}h}{\bar{\mathrm{d}}t}\frac{\partial(\sigma-p)}{\partial z}-\frac{\dot{\gamma}\tan\psi}{\alpha}. \tag{4.17}$$

Depth integration of (4.17) is accomplished term-by-term using Leibniz' rule and applying the traction-free surface boundary conditions $p(h)=\sigma(h)=0$, yielding

$$\frac{\bar{\mathrm{d}}(\bar{p}h)}{\bar{\mathrm{d}}t}-\frac{k}{\alpha\mu}\left[\left.\frac{\partial p}{\partial z}\right|_{z=h}+\rho_\mathrm{f}g_z\right]=\frac{\bar{\mathrm{d}}(\bar{\sigma}h)}{\bar{\mathrm{d}}t}-(\bar{\sigma}-\bar{p})\frac{\bar{\mathrm{d}}h}{\bar{\mathrm{d}}t}-2\sqrt{\bar{u}^2+\bar{v}^2}\frac{\tan\psi}{\alpha}, \tag{4.18}$$

where overbars denote depth-averaged variables, and $2\sqrt{\bar{u}^2+\bar{v}^2}/h$ is used as a linear approximation of the depth-averaged shear rate magnitude. The term $(k/\alpha\mu)\rho_\mathrm{f}g_z$ arises in (4.18) from depth integration of the pore-pressure diffusion term in (4.17) and application of a zero-flux basal boundary condition stipulating that the pore-pressure gradient at the bed is hydrostatic:

$[\partial p/\partial z]_{z=0} = -\rho_f g_z$. The term $(\bar{\sigma} - \bar{p})\bar{\mathrm{d}}h/\bar{\mathrm{d}}t$ arises from depth integrating the term that includes $\partial(\sigma - p)/\partial z$ in (4.17) by parts. This term cancels some other terms and thereby reduces (4.18) to

$$\frac{\bar{\mathrm{d}}\bar{p}}{\bar{\mathrm{d}}t} - \frac{k}{\alpha\mu h}\left[\left.\frac{\partial p}{\partial z}\right|_{z=h} + \rho_f g_z\right] = \frac{\bar{\mathrm{d}}\bar{\sigma}}{\bar{\mathrm{d}}t} - 2\sqrt{\bar{u}^2 + \bar{v}^2}\frac{\tan\psi}{h\alpha}. \tag{4.19}$$

Equation (4.19) retains two pore-pressure variables, p and $\bar{p}$, however, rather than the desired single variable, p_b.

To express (4.19) in terms of p_b, we find substitutions for $\bar{p}$ and $[\partial p/\partial z]_{z=h}$ that are consistent with our assumption that m is uniform at all depths below $z = h$. This condition implies that $\nabla \cdot \boldsymbol{v}_s$ and $\nabla \cdot \boldsymbol{q}$ are not functions of z, further implying that $\partial^2 p/\partial z^2$ is not a function of z in (4.16) and (4.17). With this restriction, we solve $\partial^2 p/\partial z^2 = \text{const.}$ and employ the zero-flux basal boundary condition ($[\partial p/\partial z]_{z=0} = -\rho_f g_z$) and pressure-free surface boundary condition $p(h) = 0$ to find that $p(z, t)$ satisfies the quadratic equation

$$p(z,t) = p_b\left[1 - \left(\frac{z}{h}\right)^2\right] - \rho_f g_z h\left[\frac{z}{h} - \left(\frac{z}{h}\right)^2\right]. \tag{4.20}$$

This equation indicates how $p(z, t)$ is represented by evolving values of the basal pressure $p_b(t)$ and flow thickness $h(t)$ (figure 8). Integration and differentiation of (4.20) show that the equation also implies that

$$\bar{p} = \tfrac{2}{3}p_b - \tfrac{1}{6}\rho_f g_z h \tag{4.21}$$

and

$$\left.\frac{\partial p}{\partial z}\right|_{z=h} = -\frac{2p_b}{h} + \rho_f g_z. \tag{4.22}$$

Substitution of (4.21) and (4.22) into (4.19) then yields an equation describing evolution of basal pore-fluid pressure

$$\frac{\bar{\mathrm{d}}p_b}{\bar{\mathrm{d}}t} + \frac{3k}{\alpha\mu h^2}[p_b - \rho_f g_z h] = \frac{1}{4}\rho_f g_z\frac{\bar{\mathrm{d}}h}{\bar{\mathrm{d}}t} + \frac{3}{2}\frac{\bar{\mathrm{d}}\bar{\sigma}}{\bar{\mathrm{d}}t} - 3\sqrt{\bar{u}^2 + \bar{v}^2}\frac{\tan\psi}{h\alpha}. \tag{4.23}$$

To eliminate time derivatives on the right-hand side of (4.23), we estimate $\bar{\sigma}$ as half the basal total normal traction defined by (4.14), $\bar{\sigma} = (1/2)\rho g_z h$, and we use (4.4) and (4.6) to obtain $\bar{\mathrm{d}}(\rho h)/\bar{\mathrm{d}}t = -\rho h(\partial\bar{u}/\partial x + \partial\bar{v}/\partial y)$ and $\bar{\mathrm{d}}h/\bar{\mathrm{d}}t = D[(\rho - \rho_f)/\rho] - h(\partial\bar{u}/\partial x + \partial\bar{v}/\partial y)$. These substitutions, in addition to the substitution $\tan\psi = m - [m_{crit}/(1 + \sqrt{N})]$ from (3.22), yield the pore-pressure evolution equation we use in our model

$$\begin{aligned}\frac{\bar{\mathrm{d}}p_b}{\bar{\mathrm{d}}t} + \frac{3k}{\alpha\mu h^2}[p_b - \rho_f g_z h] \\ = \frac{\rho_f g_z}{\rho}\left[\frac{D(\rho - \rho_f)}{4}\right] - \frac{(\rho_f + 3\rho)g_z h}{4}\left[\frac{\partial\bar{u}}{\partial x} + \frac{\partial\bar{v}}{\partial y}\right] - \frac{3\sqrt{\bar{u}^2 + \bar{v}^2}}{h\alpha}\left[m - \frac{m_{crit}}{1 + \sqrt{N}}\right].\end{aligned} \tag{4.24}$$

Assessment of the depth-averaged value of N in (4.24) employs the depth-averaged shear rate estimate $\dot{\gamma} = 2\sqrt{\bar{u}^2 + \bar{v}^2}/h$, which assumes a linear bed-normal velocity profile.

A direct connection between p_b and the dilation rate D can be established by using (3.28), (4.2), and the pore-pressure distribution described by (4.20) to find that

$$D = -\frac{2k}{\mu h}[p_b - \rho_f g_z h]. \tag{4.25}$$

This relationship provides closure to the model. It also shows that p_b influences all of the other dependent variables in the model, because each of the depth-averaged evolution equations (4.6), (4.7), (4.11) and (4.12) contains a source term involving D. This influence can be viewed in a different light by combining (4.25) with (4.22) and (3.26) to obtain

$$D = -q_z|_{z=h}, \tag{4.26}$$

where $q_z|_{z=h}$ is the specific discharge (positive upward) of fluid moving through the surface at $z = h$ during dilation or contraction (figure 7). Thus, in our model the dilation rate, excess basal

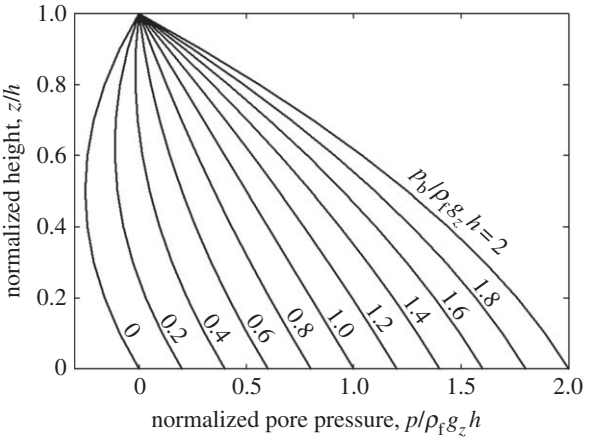

Figure 8. Graph of equation (4.20), illustrating a sequence of instantaneous pore-pressure profiles that satisfy imposed boundary conditions and the constraint $\partial^2 p/\partial z^2 = \text{const.}$ as the normalized basal pore pressure $p_b/\rho_f g_z h$ evolves. As $p_b/\rho_f g_z h \to 0$, pore pressures become negative at heights $0 < z < h$, implying the existence of a tension-saturated state.

pore pressure and fluid flux through the virtual free surface are different manifestations of the same phenomenon.

The relationships expressed by (4.25) and (4.26) are contingent on our assumption that all debris, except that passing through the virtual free surface, remains fully saturated with liquid. This assumption would be violated if debris were to dilate so rapidly that the liquid phase cavitates. Energy requirements for creation of liquid–gas interfaces in porous media tend to mitigate against this behaviour [55], but they do not preclude it. Our model does not attempt to simulate air entry and instead enforces the restriction that $p_b \geq 0$, which, according to (4.25), effectively limits D to the range $D \leq (2k/\mu)\rho_f g_z$. The model implies that small negative fluid pressures (i.e. tension-saturated zones) can develop internally as $p_b \to 0$, however (figure 8).

(d) Stress estimation

Our estimates of stress components in (4.11) and (4.12) assume that Coulomb friction in the granular fraction of the debris is fully engaged if driving forces per unit area ($\rho g_x h$ and $\rho g_y h$ in (4.11) and (4.12)) equal or exceed the sum of the other right-hand side terms in (4.11) and (4.12). If $\rho g_x h$ and $\rho g_y h$ do not suffice to fully engage Coulomb friction, then the debris is static and the stress state is indeterminate—as it is in classical limit-equilibrium methods of slope-stability analysis. To obtain a formula for the fully engaged basal shear traction, we combine (3.31) with (4.16) to model the Coulomb component of the traction, and then add a term derived from (3.25) to account for depth-integrated viscous shear resistance of fluid in the volume fraction $1 - m$. The resulting formulae for the basal shear tractions in the x- and y-directions are

$$\tau_{zx}(0) = \frac{\bar{u}}{\sqrt{\bar{u}^2 + \bar{v}^2}} \left\{ [\rho g h \cos\theta_x - p_b] \tan(\phi + \psi) + (1 - m)\mu \frac{2\bar{u}}{h} \right\} \tag{4.27}$$

and

$$\tau_{zy}(0) = \frac{\bar{v}}{\sqrt{\bar{u}^2 + \bar{v}^2}} \left\{ [\rho g h \cos\theta_y - p_b] \tan(\phi + \psi) + (1 - m)\mu \frac{2\bar{v}}{h} \right\}, \tag{4.28}$$

where θ_x and θ_y are the x and y components of the slope angle θ, and $2\bar{u}/h$ and $2\bar{v}/h$ are linear estimates of the x and y components of the fluid shear rate. In (4.27) and (4.28), the leading factors $\bar{u}/\sqrt{\bar{u}^2 + \bar{v}^2}$ and $\bar{v}/\sqrt{\bar{u}^2 + \bar{v}^2}$ ensure that $\tau_{zx}(0)$ and $\tau_{zy}(0)$ resist motion in the direction given by the vector sum of $\bar{u}$ and $\bar{v}$.

Typically, the viscous terms in (4.27) and (4.28) account for little of the total basal shear traction. For example, in a scenario with hydrostatic basal pore pressure and the values $h = 1\,\mathrm{m}$ and $\sqrt{\bar{u}^2 + \bar{v}^2} = 10\,\mathrm{m\,s^{-1}}$, the Coulomb contribution to the basal shear traction is roughly $(\rho - \rho_f)gh\cos\theta \sim 10^4\,\mathrm{Pa}$, whereas the viscous contribution is roughly 0.1 to 1 Pa. Thus, in our model the main effect of the viscous shear traction is to maintain finite basal flow resistance if complete liquefaction occurs (i.e. if $p_b = \rho g_z h$). Dissipation associated with inelastic grain collisions may contribute additional flow resistance. For the sake of parsimony, we do not include this effect in our model, although experiments indicate that the effect can be mimicked by treating ϕ as a rate-dependent quantity [39].

We represent the solid- and fluid-phase contributions to the lateral stress gradient terms $\partial(\bar{\tau}_{xx}h)/\partial x$ and $\partial(\bar{\tau}_{yy}h)/\partial y$ by using the effective stress definition (3.7) and formulae derived from this definition by Iverson & Denlinger [27]. This approach is predicated on the assumption that the lateral normal stress components τ_{xx} and τ_{yy} are each proportional to τ_{zz}, leading to the expressions

$$\frac{\partial(\bar{\tau}_{xx}h)}{\partial x} = \kappa h\frac{\partial}{\partial x}(\rho g_z h - p_b) + h\frac{\partial p_b}{\partial x} \tag{4.29}$$

and

$$\frac{\partial(\bar{\tau}_{yy}h)}{\partial y} = \kappa h\frac{\partial}{\partial y}(\rho g_z h - p_b) + h\frac{\partial p_b}{\partial y}. \tag{4.30}$$

In these equations, the terms involving gradients of $\rho g_z h - p_b$ account for lateral effective normal stresses acting in the granular phase, whereas the terms $h(\partial p_b/\partial x)$ and $h(\partial p_b/\partial y)$ account for fluid pressure contributions to the lateral stress. Additional terms can be added to (4.29) and (4.30) to account for depth-averaged deviatoric fluid normal stresses (cf. [27]), but for plausible values of the fluid viscosity μ these terms are negligible, and we exclude them here.

The granular components of the lateral normal stress terms in (4.29) and (4.30) involve a lateral pressure coefficient κ, which has been discussed at length previously [27,102–104]. For an ideal fluid, $\kappa = 1$ applies, and in this case (4.29) and (4.30) reduce to conventional forms used in shallow-water theory. Similarly, if a fully liquefied state exists (i.e. $p_b = \rho g_z h$), then (4.29) and (4.30) reduce to the conventional shallow-water form. On the other and, for a uniform slab of unliquefied Coulomb material that undergoes elongation or compression as well as basal sliding, theory indicates that κ has one of two values given by (see [5], for a derivation)

$$\kappa = 2\left[\frac{1 \pm [1 - \cos^2\phi_{int}(1 + \tan^2\phi)]^{1/2}}{\cos^2\phi_{int}}\right] - 1, \tag{4.31}$$

where ϕ is the basal friction angle and ϕ_{int} is the friction angle that describes Coulomb resistance to internal deformation. These two friction angles may or may not be the same, but $\phi \le \phi_{int}$ is necessary to ensure that basal sliding accompanies internal deformation. The larger of the two values of κ described by (4.31) is associated with compressive longitudinal deformation and always exceeds 1, whereas the smaller κ value is associated with extensional deformation and is commonly smaller than 1. Our model includes the option of using these variable κ values or, as suggested by the findings of Gray *et al.* [103,105], setting $\kappa = 1$ as a simplifying approximation.

5. Normalization and dimensionless parameters

We normalize the depth-averaged model equations by using scales appropriate for a debris flow of finite length L and thickness H (figure 6). Because downslope debris-flow motion is driven by gravitational potential, the scale for the velocity components in the x- and y-directions is $(gL)^{1/2}$, whereas the scale for the z-direction velocity component is $(gH)^{1/2}$ [102,106]. The scale $(gH)^{1/2}$ also applies for D, because $D \neq 0$ indicates relative motion of solid and liquid phases in the z-direction. The length-scale L divided by the downslope velocity scale yields the timescale for downslope debris-flow motion, $(L/g)^{1/2}$. The scale for ρ is the initial static debris bulk density ρ_0 associated with the initial solid volume fraction $m_0 : \rho_0 = m_0\rho_s + (1 - m_0)\rho_f$. The value m_0 also serves as the

scale for m. Finally, the scale for all depth-averaged stress components ($\bar{\tau}_{xx}, \bar{\tau}_{yy}, \bar{\tau}_{zz}, \bar{\tau}_{yx}, \bar{\tau}_{zx}, \bar{\tau}_{yz}$) and for the basal pore pressure p_b is $\rho_0 gH$. Use of these scales leads to definition of the following dimensionless quantities, denoted by asterisks:

$$\left.\begin{aligned} &x^* = \frac{x}{L}, \quad y^* = \frac{y}{L}, \quad z^* = \frac{z}{H}, \quad t^* = \frac{t}{(L/g)^{1/2}}, \\ &u^* = \frac{\bar{u}}{(Lg)^{1/2}}, \quad v^* = \frac{\bar{v}}{(Lg)^{1/2}}, \quad w^* = \frac{\bar{w}}{(gH)^{1/2}}, \quad h^* = \frac{h}{H}, \\ &D^* = \frac{D}{(gH)^{1/2}}, \quad m^* = \frac{m}{m_0}, \quad \rho^* = \frac{\rho}{\rho_0}, \quad p^* = \frac{p_b}{\rho_0 gH} \\ \text{and} \quad &(\tau_{xx}^*, \tau_{yy}^*, \tau_{zz}^*, \tau_{yx}^*, \tau_{zx}^*, \tau_{yz}^*) = \frac{\bar{\tau}_{xx}, \bar{\tau}_{yy}, \bar{\tau}_{zz}, \bar{\tau}_{yx}, \bar{\tau}_{zx}, \bar{\tau}_{yz}}{\rho_0 gH}. \end{aligned}\right\} \tag{5.1}$$

Substitution of (5.1) into (4.11) through (4.13) yields scaled forms of the momentum equations

$$\rho^* \left[\frac{\partial (h^* u^*)}{\partial t^*} + \frac{\partial (h^* u^{*2})}{\partial x^*} + \frac{\partial (h u^* v^*)}{\partial y^*} \right] - \varepsilon^{-1/2} \left(\rho^* - \frac{\rho_f}{\rho_0} \right) D^* u^*$$
$$= \rho^* h^* \frac{g_x}{g} + \varepsilon \left[\frac{\partial (\bar{\tau}_{yx}^* h^*)}{\partial y^*} - \frac{\partial (\bar{\tau}_{xx}^* h^*)}{\partial x^*} \right] - \tau_{zx}^*(0), \tag{5.2}$$

$$\rho^* \left[\frac{\partial (h^* v^*)}{\partial t^*} + \frac{\partial (h^* v^{*2})}{\partial y^*} + \frac{\partial (h v^* u^*)}{\partial x^*} \right] - \varepsilon^{-1/2} \left(\rho^* - \frac{\rho_f}{\rho_0} \right) D^* v^*$$
$$= \rho^* h^* \frac{g_y}{g} + \varepsilon \left[\frac{\partial (\bar{\tau}_{xy}^* h^*)}{\partial x^*} - \frac{\partial (\bar{\tau}_{yy}^* h^*)}{\partial y^*} \right] - \tau_{zy}^*(0), \tag{5.3}$$

and

$$\varepsilon^{1/2} \rho^* h^* \frac{dw^*}{dt^*} = \rho^* h^* \frac{g_z}{g} + \varepsilon \left[\frac{\partial (\bar{\tau}_{xz}^* h^*)}{\partial x^*} + \frac{\partial (\bar{\tau}_{yz}^* h^*)}{\partial y^*} \right] + \tau_{zz}^*(0), \tag{5.4}$$

where

$$\varepsilon = \frac{H}{L} \tag{5.5}$$

is a fundamental length-scale ratio that is much smaller than 1 if the shallow-flow assumption is satisfied [102,106].

The scaled mass-conservation equations (4.6) and (4.7) are

$$\rho^* \left[\frac{\partial h^*}{\partial t^*} + \frac{\partial (h^* u^*)}{\partial x^*} + \frac{\partial (h^* v^*)}{\partial y^*} \right] = \varepsilon^{-1/2} \left(\rho^* - \frac{\rho_f}{\rho_0} \right) D^* \tag{5.6}$$

and

$$\rho^* \left[\frac{\partial (h^* m^*)}{\partial t^*} + \frac{\partial (h^* u^* m^*)}{\partial x^*} + \frac{\partial (h^* v^* m^*)}{\partial y^*} \right] = \varepsilon^{-1/2} \left(-\frac{\rho_f}{\rho_0} \right) D^* m^*. \tag{5.7}$$

The scaled pore-pressure evolution equation (4.24) is

$$\frac{\bar{\mathrm{d}} p^*}{\bar{\mathrm{d}} t^*} + \frac{k(L/g)^{1/2}}{\alpha \mu H^2} \frac{3}{h^{*2}} \left[p^* - \frac{\rho_f}{\rho_0} \frac{g_z}{g} h^* \right]$$
$$= \varepsilon^{-1/2} \frac{D^*}{4\rho^*} \frac{\rho_f}{\rho_0} \frac{g_z}{g} \left(\rho^* - \frac{\rho_f}{\rho_0} \right) - \left[\frac{g_z}{g} \frac{h^*}{4} \left(\frac{\partial u^*}{\partial x^*} + \frac{\partial v^*}{\partial y^*} \right) \right] \left(3\rho^* + \frac{\rho_f}{\rho_0} \right)$$
$$- \varepsilon^{-1} (\alpha \rho_0 gH)^{-1} \frac{3\sqrt{u^{*2} + v^{*2}}}{h^*} \left[m_0 m^* - \frac{m_{crit}}{1 + \sqrt{N}} \right]. \tag{5.8}$$

Finally, the scaled version of the closure equation (4.25) is

$$D^* = \varepsilon^{1/2} \alpha \rho_0 gH \left(\frac{k(L/g)^{1/2}}{\alpha \mu H^2} \right) \left[p^* - \frac{\rho_f}{\rho_0} \frac{g_z}{g} h^* \right]. \tag{5.9}$$

Table 2. Plausible ranges of values of dimensionless model parameters for diverse debris flows.

parameter	description	range of values if $H = 0.1$ m, $L = 100$ m	range of values if $H = 10$ m, $L = 10^4$ m
m_{crit}	lithostatic critical-state solid volume fraction	0.5–0.7	0.5–0.7
ρ_f/ρ_0	ratio of pore-fluid density to initial (lithostatic) debris bulk density	0.4–0.7	0.4–0.7
ϕ	constant-volume friction angle of granular debris in contact with bed	0.5–0.8 rad	0.5–0.8 rad
$\frac{k(L/g)^{1/2}}{\alpha\mu H^2}$	ratio of timescales for downslope debris-flow motion and pore-pressure diffusion	10^{-7}–10^{4}	10^{-10}–10^{1}
$\alpha\rho_0 gH$	normalized debris compressibility	10^{-2}–1	10^{-1}–10
$\frac{\mu}{\rho_0 H(gL)^{1/2}}$	reciprocal Reynolds number for downslope motion of pore fluid	$<10^{-4}$	$<10^{-7}$

The shallow-flow assumption $\varepsilon \ll 1$ provides a basis for comparing the relative magnitudes of terms in these scaled equations. The stress gradient terms in (5.2)–(5.4) are of order ε^1, and consequently they may be negligible in many circumstances. The bed-normal acceleration term involving $\bar{\mathrm{d}}\bar{w}^*/\bar{\mathrm{d}}\bar{t}^*$ in (5.4) also is commonly negligible, because it is of order $\varepsilon^{1/2}$. All terms that contain D^* are effectively of order ε^0, because the factors $\varepsilon^{1/2}$ and $\varepsilon^{-1/2}$ in these terms cancel one another if (5.9) is substituted into (5.2), (5.3) and (5.6)–(5.8). Thus, no term containing D^* can be neglected.

Although shallow-flow scaling indicates that stress gradient terms are small, modelling surge-like motion of debris flows requires retention of the normal stress gradient terms $\partial(\tau^*_{xx}h^*)/\partial x^*$ and $\partial(\tau^*_{yy}h^*)/\partial y^*$ in (5.2) and (5.3) [102]. Our computations neglect all other terms of order ε, however—thereby distinguishing our approach from that used in some previous debris-flow and avalanche models [27,29,101]. In our model, the terms containing D^* play a more essential role, and we aim to evaluate this role without juxtaposing unnecessary complications.

The scaled model equations contain relatively few dimensionless parameters. Three of these parameters, g_x/g, g_y/g and g_z/g, reflect the extrinsic influence of the local slope angle and orientation, which are independent of the properties of the debris flow. The remaining six parameters express the influence of intrinsic debris-flow properties:

$$m_{crit}, \quad \frac{\rho_f}{\rho_0}, \quad \frac{k(L/g)^{1/2}}{\alpha\mu H^2}, \quad \alpha\rho_0 gH, \quad \phi, \quad \frac{\mu}{\rho_0 H(gL)^{1/2}}. \tag{5.10}$$

The first four of these parameters appear explicitly in equations (5.2) through (5.9), whereas the last two parameters are contained implicitly in (5.2) and (5.3) as a result of the boundary shear tractions specified in (4.27) and (4.28). Table 2 summarizes the spectrum of plausible values of the six parameters in (5.10) for both small-scale debris flows (with $H = 0.1$ m and $L = 100$ m) and large-scale flows (with $H = 10$ m and $L = 10^4$ m).

The parameter $k(L/g)^{1/2}/\alpha\mu H^2$ plays the most important role in affecting model predictions of flow behaviour, because it has values that can vary by many orders of magnitude, even in flows of fixed size (table 2). (Values of the parameter $\mu/\rho_0 H(gL)^{1/2}$ also can range widely, but they are universally small, indicating that viscous shearing plays a relatively minor role in resisting motion.) Model predictions also depend strongly on m_{crit}, because the value of this parameter

establishes whether the initial state of debris with $m = m_0$ is dilative ($\psi > 0$ if $m_0 > m_{crit}$) or contractive ($\psi < 0$ if $m_0 < m_{crit}$). The sign of $m_0 - m_{crit}$ consequently determines the sign of pore-pressure changes that occur during the first stages of downslope debris motion. Debris-flow size also has an important influence, because as flow size increases, values of $k(L/g)^{1/2}/\alpha\mu H^2$ decrease, whereas those of $\alpha\rho_0 gH$ increase. In summary, the behaviour of model predictions depends largely on topography, initial conditions and the value of $k(L/g)^{1/2}/\alpha\mu H^2$.

The parameter $k(L/g)^{1/2}/\alpha\mu H^2$ can be viewed as a time-scale ratio, in which $(L/g)^{1/2}$ is the timescale for downslope debris-flow motion and $\alpha\mu H^2/k$ is the timescale for pore-pressure relaxation to a hydrostatic state (cf. [54]). Within these timescales, the greatest source of variability arises from the pore-pressure diffusivity, $k/\alpha\mu$, which depends chiefly on the grain-size distribution and degree of debris dilation. A very broad range of diffusivities (10^{-7}–10^{2} m^2 s^{-1}) results from considering the full ranges of plausible values of k (10^{-13}–10^{-7} m^2), α (10^{-7}–10^{-4} Pa) and μ (10^{-3}–10^{-1} Pa-s) for debris ranging from mud-rich and gravel-poor to gravel-rich and mud-poor. The typical range of $k/\alpha\mu$ values may be considerably smaller, however. Values of $k/\alpha\mu$ determined experimentally for quasi-static debris-flow materials with compositions dominated by mud or by sand and gravel have ranged only from about 10^{-7} to 10^{-4} m^2 s^{-1} [5,61,68,72].

6. Discussion

Our model comprises a set of five simultaneous partial differential equations describing coupled evolution of $\bar{u}(x,y,t)$, $\bar{v}(x,y,t)$, $h(x,y,t)$, $m(x,y,t)$ and $p_b(x,y,t)$. A concise recapitulation of these equations and ancillary constitutive formulae is provided in our companion paper [46].

Application of our model typically entails simulating debris-flow motion that begins from a statically balanced initial state with $\bar{u} = \bar{v} = 0$. In such stable states, basal pore pressures $p_b(x,y,t)$ are by definition too small to satisfy (4.27) or (4.28) together with (4.29) or (4.30). Motion can then be triggered either by gradually increasing p_b (simulating the effect of rainfall or snowmelt infiltration), gradually reducing the basal friction angle, ϕ (simulating the effects of rock weathering or decay of roots that help bind soil), gradually changing the slope geometry (simulating erosion or human intervention) or rapidly changing $\boldsymbol{g}$ (simulating earthquakes). In all scenarios, motion begins when and where an infinitesimal force imbalance first develops. In this way, the model simulates the onset of slope instability and a transition to dynamic behaviour that may or may not entail rapid flow—contingent on dilatancy and pore-pressure feedback.

The model's representation of flow dynamics can be compared with that of some better-established models. For example, the depth-averaged evolution equations reduce to a form like that of the Savage–Hutter [102] granular avalanche model if the dilatancy, compressibility and pore-fluid viscosity and density are zero, implying that the restrictions D=0, $m = m_0 = m_{crit}$ and p_b=0 are enforced. On the other hand, if the restrictions $D = 0$, $m = m_0 = m_{crit}$, $\rho = \rho_f$ and ϕ=0 apply, the equations provide a conventional description of shallow-water flow. In this case, the debris behaves as an incompressible liquid, and the pore-pressure evolution equation (4.24) reduces to the hydrostatic balance $p_b = \rho g_z h$. Moreover, the longitudinal stress gradients given by (4.29) and (4.30) reduce to $\rho g_z h(\partial h/\partial x)$ and $\rho g_z h(\partial h/\partial y)$, and the basal shear tractions given by (4.27) and (4.28) contain only viscous components that represent fluid effects. In shallow-water models, these basal tractions can be approximated in a variety of other ways in an effort to account for the effects of turbulence.

Behaviour that temporarily or locally mimics shallow-water flow can occur as D, m and ρ evolve in our model, provided that $k(L/g)^{1/2}/\alpha\mu H^2 \ll 1$ and $m < m_{eq}$ apply. In this case, contractive shear deformation produces a persistent state of near-liquefaction because debris-flow motion occurs much more rapidly than pore-pressure relaxation. A caveat, however, is that elongation and thinning of a moving debris flow can reduce the effective value of H, thereby increasing the speed of pore-pressure relaxation in proportion to the change in H^2. This effect causes frictional resistance to increase where the flow thickness becomes small. As thickness approaches zero at debris-flow snouts, for example, pore pressure dissipates readily and increased friction develops.

Reduction of pore pressure and consequent growth of flow resistance also can result from increased shear rates, because increased shear rates reduce the value of m_{eq} through the action of dilatancy. Indeed, the order-ε^{-1} term on the right-hand side of (5.8) indicates that a lowest order, steady-state approximation of the physical processes represented in our model consists of a balance between the effects of dilatancy and generation of excess basal pore pressure. This balance can be expressed in dimensional terms as

$$p_b - \rho_f g_z h = -\frac{\mu h}{k}(\bar{u}^2 + \bar{v}^2)^{1/2}[m - m_{eq}]. \tag{6.1}$$

If $m < m_{eq}$ applies, then the steady state defined by (6.1) implies that $p_b - \rho_f g_z h < 0$, indicating that the effects of positive dilatancy reduce pore-fluid pressure and help stabilize motion. Faster motion promotes pore-pressure reduction not only by increasing the magnitude of $(\bar{u}^2 + \bar{v}^2)^{1/2}$ but also by reducing m_{eq}—as demonstrated in idealized experiments [82]. According to (6.1), the propensity for evolution of m to stabilize motion can also manifest itself during contractive behaviour with $m < m_{eq}$ and $p_b - \rho_f g_z h > 0$, because faster motion reduces m_{eq} and thereby reduces p_b.

In another special case, the model equations provide an approximate description of consolidation of quasi-static debris-flow deposits. In this case, all velocities vanish, and the pore-pressure evolution equation (4.24) reduces to

$$\frac{\bar{d}p_b}{\bar{d}t} + \frac{3k}{\alpha\mu h^2}(p_b - \rho_f g_z h) = \frac{\rho_f g_z h}{4}\frac{\rho - \rho_f}{\rho}\left[-\frac{2k}{\mu h^2}(p_b - \rho_f g_z h)\right], \tag{6.2}$$

which employs the expression for D given by (4.26). Equation (6.2) has a particularly simple solution if h and ρ are assumed to be constants, as is typically assumed in soil consolidation modelling

$$\frac{p_b - \rho_f g_z h}{p_b(0) - \rho_f g_z h} = \exp\left\{\frac{-kt}{\alpha\mu h^2}\left[3 + \left(\frac{\alpha\rho_f g_z h}{2}\right)\left(\frac{\rho - \rho_f}{\rho}\right)\right]\right\}. \tag{6.3}$$

This solution describes exponential relaxation of the basal pore pressure towards the hydrostatic equilibrium value $\rho_f g_z h$, and it satisfies the initial condition $p_b = p_b(0)$. The relaxation coefficient in (6.3) has a complicated form, but in general $(\alpha\rho_f g_z h/2)[(\rho - \rho_f)/\rho] \ll 3$ applies for all but the largest debris flows. Therefore, a useful approximation of (6.3) is

$$\frac{p_b - \rho_f g_z h}{p_b(0) - \rho_f g_z h} \approx e^{-3kt/\alpha\mu h^2}. \tag{6.4}$$

In this relationship, the basal pore-pressure relaxation time equals one-third of the pore-pressure diffusion timescale, $\alpha\mu h^2/k$. In a depth-averaged sense, this exponential decay approximates pore-pressure relaxation predicted by classical soil consolidation theory (figure 9). As excess basal pore pressures relax, quasi-static debris becomes progressively more rigid.

The pore-pressure relaxation timescale has another important implication, which arises from its relationship to the relaxation rate of m. The relaxation $m \to m_{eq}$ has a characteristic timescale $1/m_{eq}\dot{\gamma}$ that typically equals a few seconds or less if pore pressure is absent. By contrast, pore-pressure relaxation in the absence of dilatancy has a characteristic timescale $\alpha\mu h^2/k$ that typically ranges from a few minutes to many months. Owing to these disparate timescales and the strong coupling of m and p_b, the relaxation $m \to m_{eq}$ can proceed only as rapidly as the relaxation $p_b \to \rho_f g_z h$ permits. In this way, the model equations mirror experimental findings demonstrating that coupled evolution of pore space and pore-fluid pressure plays a dominant role in regulating debris-flow dynamics [16,65].

Complications that are not addressed by the model include several related to evolution of m. For example, $dm/dt < 0$ might occur near the surface of a debris flow while $dm/dt > 0$ occurs near the bed, yielding a commensurately variable pore-pressure response. Moreover, the value of m_{crit} might evolve in response to a variety of factors identified in quasi-static soil tests [10,23, 108,109]. Our aim is to omit rather than include complicating factors wherever possible, however,

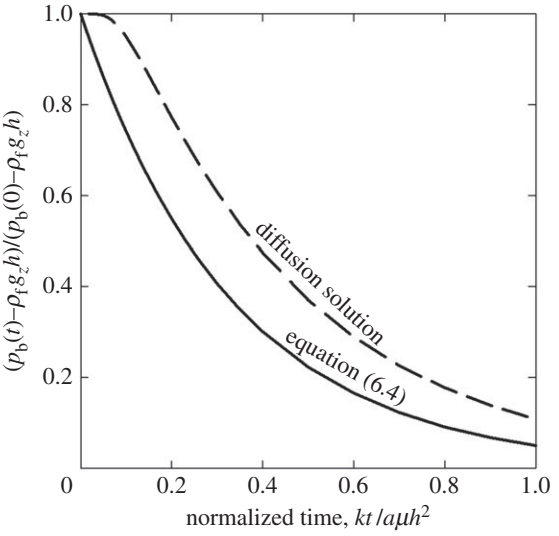

Figure 9. Graphs comparing the prediction of $p_b(t)$ given by equation (6.4) with the prediction given by an exact solution of the pore-pressure diffusion equation $\partial p/\partial t = (k/\alpha\mu)\partial^2 p/\partial z^2$ for the initial condition $p(0) = p_b(0)$ and boundary conditions $[\partial p/\partial z]_{z=0} = 0$ and $p_{z=h} = 0$ [107, p. 97]; [74, p. 409]. Owing to the finite time required for significant pore-pressure relaxation to penetrate diffusively to the bed, the diffusion equation yields predictions that lag behind those of (6.4) by a normalized time offset roughly equal to $kt/\alpha\mu h^2 = 0.1$.

and we therefore assume that m_{crit} is constant. In our companion paper, we show that such a parsimonious model can make useful predictions [46].

7. Conclusion

We have derived a depth-averaged debris-flow model aimed at seamlessly simulating all stages of flow behaviour, from initiation to post-depositional debris consolidation. The model formalizes the hypothesis that the evolving debris dilation rate, coupled to evolution of pore-fluid pressure, plays a primary role in regulating debris-flow dynamics. The model's representation of this role involves three key postulates. One postulate is that changes in the solid volume fraction m result from the interaction of the depth-averaged shear rate, dilatancy and effective stress. In turn, the evolving dilatancy angle ψ obeys $\tan\psi = m - m_{eq}$, where the equilibrium solid volume fraction m_{eq} depends on the ambient stress state and shear rate. The second key postulate, interrelated with the first, is that a Darcy drag formula describes the effect of solid–fluid interactions on the relaxation of m towards m_{eq}. The third postulate is that flow resistance is dominated by basal Coulomb friction, which is affected by dilatancy and by pore-fluid pressure mediated by Darcy drag. The Darcy and Coulomb postulates are consistent with behaviour observed previously in replicable experiments [16,61,65]. Therefore, relationships involving dilatancy represent the primary new hypothesis embodied by the model. The fact that dilatancy produces a leading-order effect in the normalized model equations enhances the prospects for conclusive model tests.

The normalized model equations contain only one dimensionless parameter that varies significantly among debris flows with differing compositions and sizes, $k(L/g)^{1/2}/\alpha\mu H^2$. Therefore, model predictions require little calibration. A typical debris-flow simulation might employ values of other dimensionless model parameters estimated as $\phi \approx 0.7$, $\rho_f/\rho_0 \approx 0.6$, $m_{crit} \approx 0.6$, $\alpha\rho_0 gH \approx 0.1$ and $\mu/\rho_0 H(gL)^{1/2} \approx 10^{-6}$. If these values are fixed, then variations in predicted debris-flow behaviour depend only on variations in the value of $k(L/g)^{1/2}/\alpha\mu H^2$ and on the initial value of $m - m_{crit}$ (in addition to extrinsic factors such as the geometry of the debris-flow source area and path). In stringent model tests, such as those performed in flume

experiments, values of these parameters can be constrained by independent measurements of material properties [16,65]. In scenarios that lack such constraints, the initial value of $m - m_{crit}$ and the value of $k(L/g)^{1/2}/\alpha\mu H^2$ may be used as calibration parameters or as stochastic variables in probabilistic forecasting.

The key role played by the time-scale ratio $k(L/g)^{1/2}/\alpha\mu H^2$ implies that debris-flow mobility predicted by our model involves inherent scale-dependence. For flows of varying size but fixed aspect ratio H/L, the motion timescale $(L/g)^{1/2}$ grows as $L^{1/2}$, whereas the pore-pressure relaxation timescale grows as H^2. Thus, large flows can retain high pore pressures longer than can small flows of similar composition. Consequent reduction of effective basal friction can help explain the extraordinarily high mobility exhibited by many large debris flows [5].

The structure of our model implies that if contractive initial conditions with $m < m_{crit}$ exist, then slope failure leads to positive pore-pressure feedback, making partial liquefaction and runaway debris-flow motion almost inevitable. On the other hand, dilative initial conditions with $m > m_{crit}$ lead to negative pore-pressure feedback. This feedback may lead to slow or intermittent landslide motion [19], but it does not preclude debris-flow initiation. According to our model, however, debris-flow initiation that commences with dilative deformation is a relatively gradual process that does not involve abrupt liquefaction and runaway behaviour. Progressive destruction of soil aggregates during the early stages of shearing can promote this type of flow initiation by causing a transition from dilative to contractive behaviour [10]. This complication, as well as complications due to grain-size segregation and entrainment of boundary material, remains to be incorporated in our model.

References

1. Jakob M, Hungr O (eds). 2005 *Debris-flow hazards and related phenomena*. Chichester, UK: Springer.
2. Takahashi T. 2007 *Debris flow mechanics, prediction and countermeasures*. London, UK: Taylor and Francis.
3. Major JJ, Pierson TC. 1992 Debris flow rheology: experimental analysis of fine-grained slurries. *Water Resour. Res.* **28**, 841–857. (doi:10.1029/91WR02834)
4. Coussot P. 1995 Structural similarity and transition from Newtonian to non-Newtonian behavior for clay-water suspensions. *Phys. Rev. Lett.* **74**, 3971–3974. (doi:10.1103/PhysRevLett.74.3971)
5. Iverson RM. 1997 The physics of debris flows. *Rev. Geophys.* **35**, 245–296. (doi:10.1029/97RG00426)
6. Martosudarmo SY, Johnson AM. 1997 Ability of muddy debris to remain mobile at low flow rates. In *Debris-flow hazards mitigation: mechanics, prediction, and assessment* (ed. C-L Chen), pp. 454–463. New York, NY: ASCE.
7. Kaitna R, Palucis MC, Tewoldebrhan B, Hill KC, Dietrich WE. 2011 The effect of fines and grain-size distribution on pore-fluid pressure, shear rate, and bulk flow resistance in large-scale experimental debris flows. Abstract, EP31C-0832, American Geophysical Union Fall Meeting, 2011.
8. Costa JE, Williams GP. 1984 *Debris-flow dynamics* (*videotape*). US. Geological Survey Open-file Report 84–606.
9. Logan M, Iverson RM. 2007 *Video documentation of experiments at the USGS debris-flow flume, 1992–2006*. US. Geological Survey Open-file Report 2007–1315. See http://pubs.usgs.gov/of/2007/1315/.
10. Iverson NR, Mann JE, Iverson RM. 2010 Effects of soil aggregates on debris-flow mobilization: results from ring-shear experiments. *Eng. Geol.* **114**, 84–92. (doi:10.1016/j.enggeo.2010.04.006)
11. Iverson RM. 2003 The debris-flow rheology myth. In *Debris-flow hazards mitigation: mechanics, prediction, and assessment*, vol. 1 (eds D Rickenmann, CL Chen), pp. 303–314. Rotterdam, The Netherlands: Millpress.
12. McDougall, Hungr. 2004. A model for the analysis of rapid landslide motion across three-dimensional terrain. *Can. Geotech. J.* **41**, 1084–1097. (doi:10.1139/t04-052)

13. Sheridan MF, Stinton AJ, Patra A, Pitman EB, Bauer A, Nichita CC. 2005 Evaluating Titan2D mass-flow model using the 1963 Little Tahoma Peak avalanches, Mount Rainier, Washington. *J. Volc. Geotherm. Res.* **139**, 89–102. (doi:10.1016/j.jvolgeores.2004.06.011)
14. Medina V, Hürlimann M, Bateman A. 2008 Application of FLATmodel, a 2D finite volume code, to debris flows in the northeastern part of the Iberian Peninsula. *Landslides* **5**, 127–142. (doi:10.1007/s10346–007–0102–3)
15. Iverson RM, Reid ME, LaHusen RG. 1997 Debris-flow mobilization from landslides. *Ann. Rev. Earth Planet. Sci.* **25**, 85–138. (doi:10.1146/annurev.earth.25.1.85)
16. Iverson RM, Reid ME, Iverson NR, LaHusen RG, Logan M, Mann JE, Brien DL. 2000 Acute sensitivity of landslide rates to initial soil porosity. *Science* **290**, 513–516. (doi:10.1126/science.290.5491.513)
17. Sassa K, Wang G-H. 2005 Mechanism of landslide-triggered debris flows: liquefaction phenomena due to the undrained loading of torrent deposits. In *Debris-flow hazards and related phenomena* (eds M Jakob, O Hungr), pp. 81–104. Chichester, UK: Springer.
18. Iverson RM. 2005 Regulation of landslide motion by dilatancy and pore pressure feedback. *J. Geophys. Res.* **110**, F02015. (doi:10.1029/2004JF000268)
19. Schaeffer DG, Iverson RM. 2008 Steady and intermittent slipping in a model of landslide motion regulated by pore-pressure feedback. *SIAM J. Appl. Math.* **69**, 769–786. (doi:10.1137/07070704X)
20. Reynolds O. 1885 On the dilatancy of media composed of rigid particles in contact with experimental illustrations. *Phil. Mag.* **2**, 469–481. (doi:10.1080/14786448508627791)
21. Reynolds O. 1886 Dilatancy. *Nature* **33**, 429–430.
22. Schofield AN, Wroth P. 1968 *Critical state soil mechanics*. New York, NY: McGraw-Hill.
23. Bolton MD. 1986 The strength and dilatancy of sands. *Geotechnique* **36**, 65–78. (doi:10.1680/geot.1986.36.1.65)
24. Houlsby GT. 1991 How the dilatancy of soils affects their behavior. In *Proc. Tenth European Conf. on Soil Mechanics and Foundation Engineering, 27–30 May, Florence, Italy*, vol. 4, pp. 1189–1202. Soil Mechanics Report Number 121/91. Oxford, UK: University of Oxford.
25. Forterre Y, Pouliquen O. 2008 Flows of dense granular media. *Ann. Rev. Fluid Mech.* **40**, 1–24. (doi:10.1146/annurev.fluid.40.111406.102142)
26. Bozhinskiy A, Nazarov A. 2000 Two-phase model of debris-flow. In *Debris-flow hazards mitigation: mechanics, prediction and assessment* (eds GF Wieczorek, ND Naeser), pp. 263–269. Rotterdam, The Netherlands: Balkema.
27. Iverson RM, Denlinger RP. 2001 Flow of variably fluidized granular masses across three-dimensional terrain: 1. Coulomb mixture theory. *J. Geophys. Res.* **106**, 537–552. (doi:10.1029/2000JB900329)
28. Savage SB, Iverson RM. 2003 Surge dynamics coupled to pore-pressure evolution in debris flows. In *Debris-flow hazards mitigation: mechanics, prediction, and assessment*, vol. 1 (eds D Rickenmann, C-L Chen), pp. 503–514. Rotterdam, The Netherlands: Millpress.
29. Pitman EB, Le L. 2005 A two-fluid model for avalanche and debris flow. *Phil. Trans. R. Soc. A* **363**, 1573–1601. (doi:10.1098/rsta.2005.1596)
30. Pudasaini SP, Wang Y, Hutter K. 2005 Modelling debris flows down general channels. *Nat. Hazards Earth Syst. Sci.* **5**, 799–819. (doi:10.5194/nhess-5-799-2005)
31. Pelanti M, Bouchut F, Mangeney A. 2008 A Roe-type scheme for two-phase shallow granular flows over variable topography. *Math. Model. Num. Anal.* **42**, 851–885. (doi:10.1051/m2an:2008029)
32. Berzi D, Jenkins JT, Larcher M. 2010 Debris flows: recent advances in experiments and modeling. *Adv. Geophys.* **52**, 103–138. (doi:10.1016/S0065-2687(10)52002-8)
33. Meruane C, Tamburrino A, Roche O. 2010 On the role of the ambient fluid on gravitational granular flow dynamics. *J. Fluid Mech.* **648**, 381–404. (doi:10.1017/S0022112009993181)
34. Pudasaini SP. 2012 A general two-phase debris-flow model. *J. Geophys. Res.* **117**, F002186. (doi:10.1029/2011JF002186)
35. Kowalski J, McElwaine JN. 2013 Shallow two-component gravity-driven flows with vertical variation. *J. Fluid Mech.* **714**, 434–462. (doi:10.1017/jfm.2012.489)
36. Jaeger HM, Nagel SR, Behringer RP. 1996 Granular solids, liquids and gases. *Rev. Mod. Phys.* **68**, 1259–1273. (doi:10.1103/RevModPhys.68.1259)
37. Aranson IS, Tsimring LS. 2002 Continuum theory of partially fluidized granular flows. *Phys. Rev. E* **65**, e61303. (doi:10.1103/PhysRevE.65.061303)

38. Pailha M, Pouliquen O. 2009 A two-phase flow description of the initiation of underwater granular avalanches. *J. Fluid Mech.* **633**, 115–135. (doi:10.1017/S0022112009007460)
39. Boyer F, Guazzelli E, Pouliquen O. 2011 Unifying suspension and granular rheology. *Phys. Rev. Lett.* **107**, 188301. (doi:10.1103/PhysRevLett.107.188301)
40. George DL. 2011 Adaptive finite volume methods with well-balanced Riemann solvers for modeling floods in rugged terrain: application to the Malpasset dam-break flood (France, 1959). *Int. J. Num. Meth. Fluids* **66**, 1000–1018. (doi:10.1002/fld.2298)
41. LeVeque RJ, George DL, Berger MJ. 2011 Tsunami modeling with adaptively refine finite-volume methods. *Acta Numerica* **20**, 211–289. (doi:10.1012/S09624929111000043)
42. McArdell BW, Partlet P, Kowalski J. 2007 Field observations of basal forces and fluid pore pressure in a debris flow. *Geophys. Res. Let.* **34**,L07406. (doi:10.1029/2006GL029183)
43. Berger C, McArdell BW, Schlunegger F. 2011 Direct measurement of channel erosion by debris flows, Illgraben, Switzerland. *J. Geophys. Res.* **116**, F01002. (doi:10.1029/2010JF001722)
44. Johnson CG, Kokelaar BP, Iverson RM, Logan M, LaHusen RG, Gray JMNT. 2012 Grain-size segregation and levee formation in geophysical mass flows. *J. Geophys. Res.* **117**, F002185. (doi:10.1029/2011JF002185)
45. McCoy SW, Kean JW, Coe JA, Tucker GE, Staley DM, Wasklewicz TA. 2012 Sediment entrainment by debris flows: *in situ* measurements from the headwaters of a small catchment. *J. Geophys. Res.* **117**, F03016. (doi:10.1029/2011JF002278)
46. George DL, Iverson RM. 2014 A depth-averaged debris-flow model that includes the effects of evolving dilatancy. II. Numerical predictions and experimental tests. *Proc. R. Soc. A* **470**, 20130820. (doi:10.1098/rspa.2013.0820)
47. Iverson RM, Reid ME, Logan M, LaHusen RG, Godt JW, Griswold JG. 2011 Positive feedback and momentum growth during debris-flow entrainment of wet bed sediment. *Nat. Geosci.* **4**, 116–121. (doi:10.1038/NGEO1040)
48. Gray JMNT, Kokelaar BP. 2010 Large particle segregation, transport and accumulation in granular free-surface flows. *J. Fluid Mech.* **652**, 105–137. (doi:10.1017/S002211201000011X)
49. Iverson RM. 2012 Elementary theory of bed-sediment entrainment by debris flows and avalanches. *J. Geophys. Res.* **117**, F03006. (doi:10.1029/2011JF002189)
50. Aris R. 1962 *Vectors, tensors, and the basic equations of fluid mechanics*. Englewood Cliffs, NJ: Prentice-Hall.
51. Fung YC. 1965 *Foundations of solid mechanics*. Englewood Cliffs, NJ: Prentice-Hall.
52. Malvern LE. 1969 *Introduction to the mechanics of a continuous medium*. Englewood Cliffs, NJ: Prentice-Hall.
53. Bartelt P, Bühler Y, Buser O, Christen M, Meier L. 2012 Modeling mass-dependent flow regime transitions to predict the stopping and depositional behavior of snow avalanches. *J. Geophys. Res.* **117**, F01015. (doi:10.1029/2010JF001957)
54. Iverson RM, Logan M, Denlinger RP. 2004 Granular avalanches across irregular three-dimensional terrain: 2. Experimental tests. *J. Geophys. Res.* **109**, F01015. (doi:10.1029/2003JF000084)
55. Coussy O. 2010 *Mechanics and physics of porous solids*. Chichester, UK: Wiley.
56. Coussot P, Meunier M. 1996 Recognition, classification and mechanical description of debris flows. *Earth Sci. Rev.* **40**, 209–227. (doi:10.1016/0012-8252(95)00065-8)
57. Costa JE. 1984 Physical geomorphology of debris flows. In *Developments and applications of geomorphology* (eds JE Costa, PJ Fleisher), pp. 268–317. Heidelberg, Germany: Springer.
58. Bear J. 1972 *Dynamics of fluids in porous media*. New York, NY: Dover.
59. Iverson RM, Major JJ. 1986 Groundwater seepage vectors and the potential for hillslope failure and debris–flow mobilization. *Water Res. Res.* **22**, 1543–1548. (doi:10.1029/WR022i011p01543)
60. Johnson G, Massoudi M, Rajagopal KR. 1990 A review of interaction mechanisms in fluid-solid flows. Tech. Rep. DOE/PETC/TR-90/9, U.S. Dep. of Energy, 54 pp., Pittsburgh Energy Technol. Cent., Pittsburgh, PA, USA.
61. Major JJ. 2000 Gravity-driven consolidation of granular slurries—implications for debris-flow deposition and deposit characteristics. *J. Sedimentary Res.* **70**, 64–83. (doi:10.1306/2DC408FF-0E47-11D7-8643000102C1865D)
62. Lade PV, de Boer R. 1997 The concept of effective stress for soil, concrete, and rock. *Geotechnique* **47**, 61–78. (doi:10.1680/geot.1997.47.1.61)
63. Passman SL, McTigue DF. 1986 A new approach to the effective stress principle. In *Compressibility phenomena in subsidence* (ed. SK Saxena), pp. 79–91. New York, NY: Eng. Found.

64. de Boer R, Ehlers W. 1990 The development of the concept of effective stresses. *Acta Mech.* **83**, 77–92. (doi:10.1007/BF01174734)
65. Iverson RM, Logan M, LaHusen RG, Berti M. 2010 The perfect debris flow: aggregated results from 28 large-scale experiments. *J. Geophys. Res.* **115**, F03005. (doi:10.1029/2009JF001514)
66. Paik J, Son S, Kim T, Kim S. 2012 A real-scale field experiment of debris flow for investigating its deposition and entrainment. *Am. Geophys. Union*. See http://www.youtube.com/watch?v=8CHFl1fIl-c.
67. Johnson KL. 1985 *Contact mechanics*. Cambridge, UK: Cambridge University Press.
68. Major JJ, Iverson RM, McTigue DF, Macias S, Fiedorowicz BK. 1997 Geotechnical properties of debris-flow sediments and slurries. In *Debris-flow hazards mitigation: mechanics, prediction, and assessment* (ed. C-L Chen), pp. 249–259. New York, NY: ASCE.
69. Been K, Sills GC. 1981 Self-weight consolidation of soft soils: an experimental and theoretical study. *Geotechnique* **31**, 519–535. (doi:10.1680/geot.1981.31.4.519)
70. Carrier WD, Bromwell LG, Somogyi F. 1983 Design capacity of slurried mineral waste ponds. *J. Geotech. Engr.* **109**, 699–716. (doi:10.1061/(ASCE)0733-9410(1983)109:5(699))
71. Fox PJ, Baxter CDP. 1997 Consolidation properties of soil slurries from hydraulic consolidation test. *J. Geotech. Geoenviron. Eng.* **123**, 770–776. (doi:10.1061/(ASCE)1090-0241(1997)123:8(770))
72. Major JJ. 1996 Experimental studies of deposition by debris flows: process, characteristics of deposits, and effects of pore-fluid pressure, p. 339. Unpublished PhD dissertation, University of Washington, Seattle, WA, USA.
73. Yamamuro JA, Lade PV. 1997 Static liquefaction of very loose sands. *Can. Geotech. J.* **34**, 905–917. (doi:10.1139/t97-057)
74. Lambe TW, Whitman RV. 1979 *Soil mechanics, SI version*. New York, NY: Wiley.
75. Janda RJ, Scott KM, Nolan KM, Martinson HA. 1981 Lahar movement, effects, and deposits. In *The 1980 Eruptions of Mount St Helens, Washington* (eds PW Lipman, DR Mullineaux), pp. 461–478. US. Geological Survey Professional Paper 1250. Washington, DC: US Government Printing Office.
76. Vallance JW, Scott KM. 1997 The Osceola Mudflow from Mount Rainier: sedimentology and hazard implications of a huge clay-rich debris flow. *Geol. Soc. Am. Bull.* **109**, 143–163. (doi:10.1130/0016-7606(1997)109<0143:TOMFMR>2.3.CO;2)
77. Rowe PW. 1962 The stress-dilatancy relation for static equilibrium of an assembly of particles in contact. *Proc. R. Soc. Lond. A* **269**, 500–527. (doi:10.1098/rspa.1962.0193)
78. Nemat-Nasser S. 1980 On behavior of granular materials in simple shear. *Soils Found.* **20**, 59–73. (doi:10.3208/sandf1972.20.3_59)
79. Rao KK, Nott PR. 2008 *An introduction to granular flow*. Cambridge, UK: Cambridge University Press.
80. Bagnold RA. 1954 Experiments on a gravity-free dispersion of large solid spheres in a Newtonian fluid under shear. *Proc. R. Soc. Lond. A* **225**, 49–63. (doi:10.1098/rspa.1954.0186)
81. Hunt ML, Zenit R, Campbell CS, Brennen CE. 2002 Revisiting the 1954 suspension experiments of RA. Bagnold. *J. Fluid Mech.* **452**, 1–24.
82. Deboeuf A, Gauthier G, Martin J, Yorkovetsky Y, Morris JF. 2009 Particle pressure in a sheared suspension: a bridge from osmosis to granular dilatancy. *Phys. Rev. Lett.* **102**, 108031. (doi:10.1103/PhysRevLett.102.108301)
83. Puckett JG, Lechenault F, Daniels KE. 2011 Local origins of volume fraction fluctuations in dense granular materials. *Phys. Rev. E* **83**, 041301. (doi:10.1103/PhysRevE.83.041301)
84. Howell D, Behringer RP, Veje C. 1999 Stress fluctuations in a 2D granular Couette experiment: a continuous transition. *Phys. Rev. Lett.* **82**, 5241–5244. (doi:10.1103/PhysRevLett.82.5241)
85. Roux S, Radjai F. 1998 Texture-dependent rigid plastic behaviour. In *Proc.: physics of dry granular media, September 1997, Carg'ese, France* (eds HJ Herrmann *et al.*), pp. 305–311. Dordrecht, The Netherlands: Kluwer.
86. Ancey C, Evesque P. 2000 Frictional-collisional regime for granular suspension flows down an inclined channel. *Phys. Rev. E* **62**, 8349–8360. (doi:10.1103/PhysRevE.62.8349)
87. Cassar C, Nicolas M, Pouliquen O. 2005 Submarine granular flows down inclined planes. *Phys. Fluids* **17**, 103301-1–103301-11. (doi:10.1063/1.2069864)
88. Savage SB. 1984 The mechanics of rapid granular flows. *Adv. Appl. Mech.* **24**, 289–366. (doi:10.1016/S0065-2156(08)70047-4)
89. O'Brien JS, Julien PV. 1988 Laboratory analysis of mudflow properties. *J. Hydraul. Eng.* **114**, 877–887. (doi:10.1061/(ASCE)0733-9429(1988)114:8(877))

90. Ancey C. 2001 Role of lubricated contacts in concentrated polydisperse suspensions. *J. Rheol.* **45**, 1421–1439. (doi:10.1122/1.1413504)
91. Heller H, Keren R. 2001 Rheology of Na-rich montmorillonite suspension as affected by electrolyte concentration and shear rate. *Clays Clay Min.* **49**, 286–291. (doi:10.1346/CCMN.2001.0490402)
92. Neuman SP. 1994 Generalized scaling of permeabilities: validation and effect of support scale. *Geophys. Res. Lett.* **21**, 349–352. (doi:10.1029/94GL00308)
93. Iverson RM, LaHusen RG. 1989 Dynamic pore-pressure fluctuations in rapidly shearing granular materials. *Science* **246**, 796–799. (doi:10.1126/science.246.4931.796)
94. Ancey C, Coussot P, Evesque P. 1999 A theoretical framework for granular suspensions in a steady simple shear flow. *J. Rheol.* **43**, 1673–1699. (doi:10.1122/1.551067)
95. Rice JR, Cleary MP. 1976 Some basic stress diffusion solutions for fluid-saturated elastic porous media with compressible constituents. *Rev. Geophys.* **14**, 227–241. (doi:10.1029/RG014i002p00227)
96. Sokolovski VV. 1960 *Statics of soil media*. London, UK: Butterworths.
97. Savage SB, Sayed M. 1984 Stresses developed in dry cohesionless granular materials sheared in an annular shear cell. *J. Fluid Mech.* **142**, 391–430. (doi:10.1017/S0022112084001166)
98. Iverson RM, Vallance JW. 2001 New views of granular mass flows. *Geology* **29**, 115–118. (doi:10.1130/0091-7613(2001)029<0115:NVOGMF>2.0.CO;2)
99. Denlinger RP, Iverson RM. 2001 Flow of variably fluidized granular masses across three-dimensional terrain: 2. numerical predictions and experimental tests. *J. Geophys. Res.* **106**, 553–566. (doi:10.1029/2000JB900330)
100. Desai CS, Siriwardane HJ. 1984 *Constitutive laws for engineering materials, with emphasis on geological materials*. Englewood Cliffs, NJ: Prentice-Hall.
101. Denlinger RP, Iverson RM. 2004 Granular avalanches across irregular three-dimensional terrain: 1. Theory and computation. *J. Geophys. Res.* **109**, F01014. (doi:10.1029/2003JF000085)
102. Savage SB, Hutter K. 1989 The motion of a finite mass of granular material down a rough incline. *J. Fluid Mech.* **199**, 177–215. (doi:10.1017/S0022112089000340)
103. Gray JMNT, Wieland M, Hutter K. 1999 Free surface flow of cohesionless granular avalanches over complex basal topography. *Proc. R. Soc. Lond. A* **455**, 1841–1874. (doi:10.1098/rspa.1999.0383)
104. Pudasaini SP, Hutter K. 2007 *Avalanche dynamics*. Berlin, Germany: Springer.
105. Gray JMNT, Tai Y-C, Noelle S. 2003 Shock waves, dead zones and particle-free regions in rapid granular free-surface flows. *J. Fluid Mech.* **491**, 161–181. (doi:10.1017/S0022112003005317)
106. Savage SB, Hutter K. 1991 The dynamics of avalanches of granular materials from initiation to runout I, Analysis. *Acta Mech.* **86**, 201–223. (doi:10.1007/BF01175958)
107. Carslaw HS, Jaeger JC. 1959 *Conduction of heat in solids*. Oxford, UK: Oxford University Press.
108. Schanz T, Vermeer PA. 1996 Angles of friction and dilatancy of sand. *Geotechnique* **46**, 145–151. (doi:10.1680/geot.1996.46.1.145)
109. Lancelot L, Shahrour I, Al Mahmoud M. 2006 Failure and dilatancy properties of sand at relatively low stresses. *J. Eng. Mech.* **132**, 1396–1399. (doi:10.1061/(ASCE)0733-9399(2006)132:12(1396))